Advanced Concept Architecture Design and Integrated Analysis (ACADIA)

Submitted to the National Institute of Aerospace (NIA) on November 3rd , 2017

Effort: October 1, 2016 – October 30, 2017

NIA Point of Contact (PoC):

Carole E. McPhillips
Deputy Contracts Manager
National Institute of Aerospace
100 Exploration Way
Hampton, VA 23666-6186
(757) 325-6762 (office)
(757) 325-6701 (fax)
carole.mcphillips@nianet.org

ASDL Technical PoC:

Dimitri Mavris
Boeing Prof. Advanced Systems Design
dimitri.mavris@aserospace.gatech.edu

Aerospace Design Laboratory
Guggenheim School of Aerospace Engineering
Georgia Institute of Technology
Atlanta, GA 30332-0150
www.asdl.gatech.edu

REPORT DOCUMENTATION PAGE

Form Approved
OMB No. 0704-0188

PLEASE DO NOT RETURN YOUR FORM TO THE ABOVE ADDRESS.

1. REPORT DATE *(DD-MM-YYYY)*	2. REPORT TYPE	3. DATES COVERED *(From - To)*
03-11-2017	Annual Research Report	20161001 - 20161030

4. TITLE AND SUBTITLE

Advanced Concept Architecture Design and Integrated Analysis (ACADIA)

5a. CONTRACT NUMBER

W911NF-16-2-0229

5b. GRANT NUMBER

5c. PROGRAM ELEMENT NUMBER

6. AUTHOR(S)

Cedric Justin, Youngjun Choi, Hee Yong Jeon, Po-Nien Lin, Minki Kim, Dimitri Mavris

5d. PROJECT NUMBER

8504

5e. TASK NUMBER

5f. WORK UNIT NUMBER

7. PERFORMING ORGANIZATION NAME(S) AND ADDRESS(ES)

Aerospace Systems Design Laboratory, Guggenheim School of Aerospace Engineering, Georgia Institute of Technology, Atlanta, GA 30332-0150

8. PERFORMING ORGANIZATION REPORT NUMBER

9. SPONSORING/MONITORING AGENCY NAME(S) AND ADDRESS(ES)

US Army Research Laboratory
RDRL-VTV
6340 Rodman Rd
Aberdeen Proving Ground, MD 21005

10. SPONSOR/MONITOR'S ACRONYM(S)

11. SPONSOR/MONITOR'S REPORT NUMBER(S)

12. DISTRIBUTION/AVAILABILITY STATEMENT

Approved for public release; distribution is unlimited.

13. SUPPLEMENTARY NOTES

Research was sponsored by the Army Research Laboratory and was accomplished under Cooperative Agreement Number W911NF-16-2-0229. The views and conclusions contained in this document are those of the authors and should not be interpreted as

14. ABSTRACT

A process is developed to enable a multi-architecture vehicle modeling process. The process starts with the identification of off-the-shelf components available for the design of small UAS. These components are characterized experimentally and to some extent a library of component models is constructed. The library is not extensive at this point since only critical components have been included. These critical components have some attributes attached to them (e.g., number of cells and capacity for a battery, mass and maximum power for a motor, and maximum thrust for a propeller). The design mission of interest to the user is analyzed next to identify pertinent design constraints and to enable the sizing of a small size autonomous vehicle. This requires models in order to properly design and analyze the performance of vehicles of differing architectures. As part of this research, three architectures have been retained: a fixed wing architecture (FW), a multicopter architecture (x-COP), and a hybrid Vertical Take Off and Landing (H-VTOL) architecture. For each of these architectures, one or more variants have been proposed (three for FW, one for x-COP, and three for H-VTOL. Many more variants of these architectures can be added by the analyst by simply supplying

15. SUBJECT TERMS

unmanned systems, design space exploration, systems engineering, integrated design and manufacturing, additive manufacturing, 3D printing, on-demand, forward deployed, conceptual design, sizing, architecture, experimentation, technology tradeoffs, fixed wing, multicopter, quad copter, mission-driven deign, sensitivity study

16. SECURITY CLASSIFICATION OF:			17. LIMITATION OF ABSTRACT	18. NUMBER OF PAGES	19a. NAME OF RESPONSIBLE PERSON
a. REPORT	b. ABSTRACT	c. THIS PAGE			Eric Spero
Unclassified	Unclassified	Unclassified	UU	60	19b. TELEPHONE NUMBER *(Include area code)* (410) 278-8743

Reset

Standard Form 298 (Rev. 8/98)
Prescribed by ANSI Std. Z39.18

Table of Contents

List of Figures

List of Tables

I. Research Objectives

The purpose of the ACADIA research effort is to advance the state of the art in the ability to make trades across architectures for small Unmanned Aerial Systems in a manner that maintains sufficient fidelity for design decision making. In other words, the process leading to the choice of one particular small UAS architecture compared to another small UAS architecture is not well understood: besides obvious performance capabilities (i.e. ability to hover), the fundamentals reasons underlying the choice of one specific architecture (for instance a multicopter) when another architecture (for instance an hybrid VTOL vehicle) with similar capability and which could also complete the mission, are poorly understood. The tradeoffs and performance penalties implicitly accepted when choosing a specific architecture need to be highlighted and adequately conveyed to decision makers to ensure that all pertinent aspects of the decision are analyzed.

In order to accomplish this, an environment enabling exploration and understanding of the capabilities of different small-sized UAS architectures across a broad set of mission parameters is envisioned. By enabling consistent fidelity analyses across multiple architectures, the environment facilitates the understanding of consequences of architectural decisions in terms of metrics of interest such as payload, range, endurance, complexity, manufacturability, hover time...

This research is therefore multi-faceted and requires that three capabilities be developed; first, the capability to model and design at the pre-conceptual level vehicles of different architectures, satisfying specific mission constraints, using off-the shelf components, and allowing a significant use of additive manufacturing; second, the capability to identify and select metrics of interest to the decision makers and to quantitatively estimate their values; finally, the capability to display the results from these previous two exercises in a dynamic environment enabling the user to gain insights and to discover tradeoffs, correlations and patterns in the results.

II. Executive Summary of Research Performed

A process is developed to enable a multi-architecture vehicle modeling process as highlighted in Figure 1. The process starts with the identification of off-the-shelf components available for the design of small UAS. These components are characterized experimentally and to some extent a library of component models is constructed. The library is not extensive at this point since only critical components have been included. These critical components have some attributes attached to them (number of cells and capacity for a battery, mass and maximum power for a motor, and maximum thrust for a propeller…). The design mission of interest to the user is analyzed next to identify pertinent design constraints and to enable the sizing of a small size autonomous vehicle. This requires models in order to properly design and analyze the performance of vehicles of differing architectures. As part of this research, three architectures have been retained: a fixed wing architecture (FW), a multicopter architecture (x-COP), and a hybrid Vertical Take Off and Landing (H-VTOL) architecture. For each of these architectures, one or more variants have been proposed (three for FW, one for x-COP, and three for H-VTOL. Many more variants of these architectures can be added by the analyst by simply supplying appropriate vehicle data. Finally, the capabilities of the different architectures are quantified using some pre-determined metrics of interest. These capabilities are presented to the decision maker in a visualization and trade-off environment which enables an exploration of the design space as well as the carrying out of sensitivity studies.

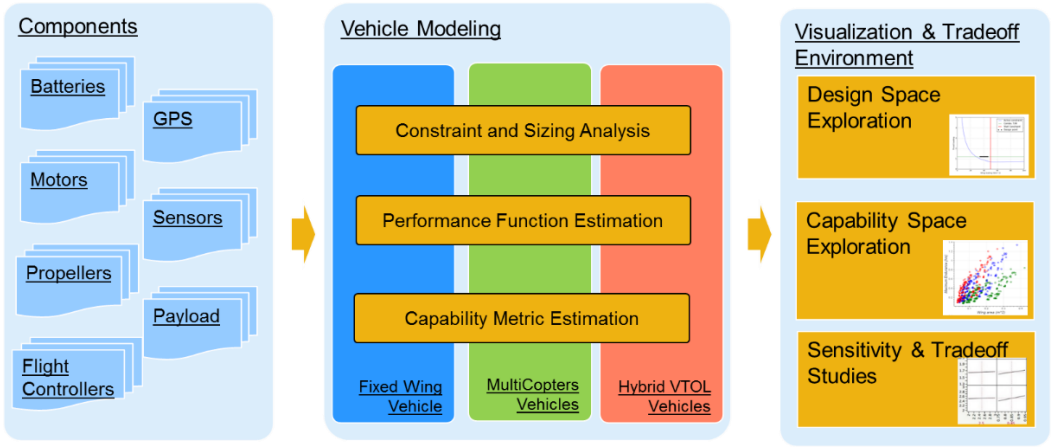

Figure 1: ACADIA Process and Methodology

Component model library

The construction of a library of component models for major components of the small vehicles has been performed and the gathering of experimental data-points to characterize the performance of commonly used batteries, motors and propeller is complete. Combinations of propellers with 5 to 16 inches diameters and motors from 480 kV to 2300 kV of motor were experimentally characterized to get data, such as maximum thrust, power, and weight. The database with the primary attributes is shown in Figure

2. A variety of 3-cell and 4-cell batteries were also collected with capacity ranging from 1500mAh to 10000mAh. The databases were stored as .CSV files in the *static* folder in the ACADIA sizing tool. No data has been gathered yet with respect to GPS, payload sensors, or flight controllers as these components are of lesser criticality for the research to be performed.

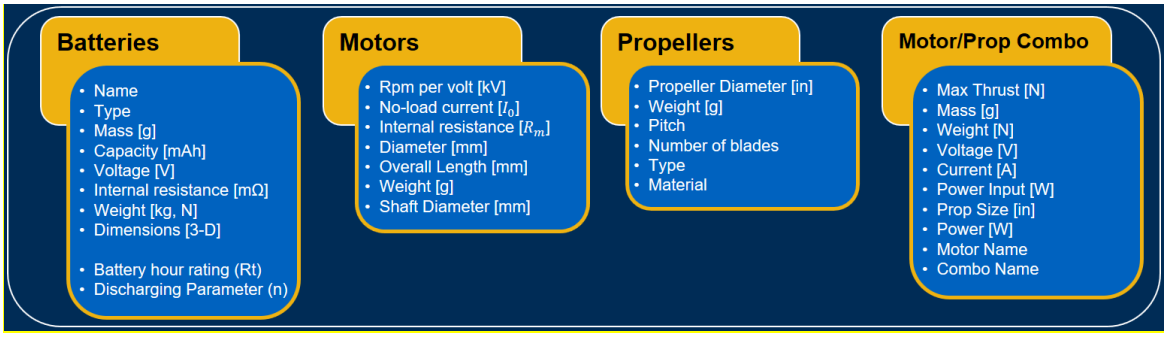

Figure 2: Primary attributes of the database of the components

Sizing and synthesis

Sizing and synthesis methods for the three vehicle architectures have been implemented and a representation of the overall sizing and synthesis process is given in Figure 3. As graphically explained in Figure 2, the process starts by using aerodynamic characteristics of pre-selected vehicle configuration (such as drag coefficient, equivalent flat plate area, aspect ratio, etc.) and motor, propeller, and battery performance data. If needed, a constraint analysis is performed to check whether the thrust and/or power installed and/or the wing area are sufficient to meet all constraints set forth by the analyst. Finally a mission analysis is performed to check whether the energy required to fly the mission can be supplied by the energy storage device on board the vehicle.

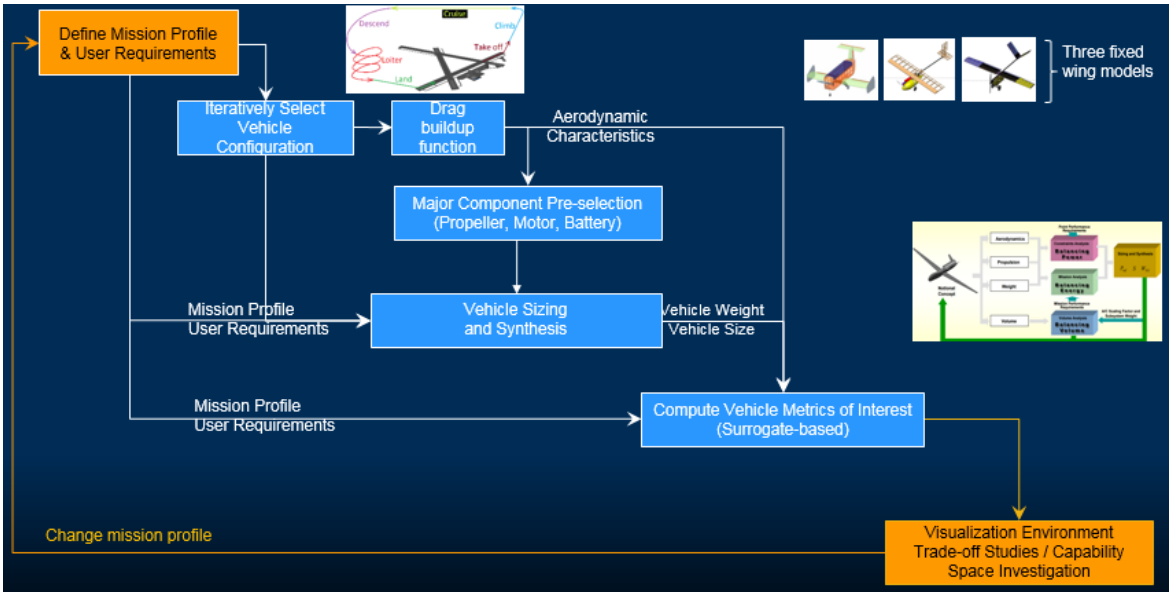

Figure 3: Multi architecture vehicle modeling process

Vehicle performance and capability modeling

The performance modeling exercise is performed for three classes of vehicles to estimate some performance and capability attributes for all designs fulfilling the original design mission requirements. Several metrics of interest have been retained, namely maximum endurance, maximum range, maximum altitude, maximum rate of climb, manufacturing time, complexity (as a measure of reliability), and packing volume for ease of deployment by end user.

III. Vehicle Sizing and Synthesis

The sizing and synthesis process consists in bringing all mission requirements together in order to scale a vehicle which essentially means estimating the vehicle weight, the vehicle required power, and the vehicle required wing area if any. It is important to remember that the sizing and synthesis exercise does not actually design a vehicle. Instead, it uses a baseline construct that is either scaled up or down in order to meet user requirements.

Fixed wing vehicle

The first category of small UAS investigated is the fixed wing architecture. Fixed wing vehicles are peculiar in the sense that selecting an appropriate combination of motors, propellers and battery is necessary but not sufficient to fully characterize the vehicle. Indeed, the selection of an appropriate wing area is as important. This may lead to several feasible designs that have the same set of components (motors, propellers, and battery) but that have very different wing sizes and therefore very different capabilities.

Constraint analysis

For the fixed wing architecture, the constraint analysis is performed using the design mission requirements. It is conducted with an energy based equation originally presented by Mattingly [1]. Equation 1 shows an adapted form of this equation for an electric vehicle and it captures the relationship between thrust loading (T/W) and wing loading (W/S). Figure 4 shows a representation of Equation 1 applied to different mission segments (such as takeoff, climb, cruise, loiter, descent, and landing) with corresponding requirements and assumptions. The thrust lapse α and the weight fraction β from the original equation are assumed to be one for this class of vehicle, which typically flies at low altitude and does not burn any fuel. The feasible design space is the space above each and every constraint line in the visual depiction of the constraints shown in Figure 4.

$$\frac{T_{SL}}{W_{TO}} = \left\{ \frac{qS}{W_{TO}} \left[K_1 \left(\frac{n}{q} \frac{W_{TO}}{S} \right)^2 + K_2 \left(\frac{n}{q} \frac{W_{TO}}{S} \right) + C_{D_o} + \frac{R}{qS} \right] + \frac{1}{V} \frac{d}{dt} \left(h + \frac{V^2}{2g_o} \right) \right\}$$

T_{SL}: Thrust at sea level
W_{TO}: Takeoff weight
S: Wing Area
K_1, K_2: Induced drag coefficient
C_{D0}: Zero lift drag coefficient
R: Resistance due to ground
V: Velocity
h: Height
g_0: Gravitational acceleration
n: Load factor
q: Dynamic pressure

Equation 1: Energy based equation constraint analysis

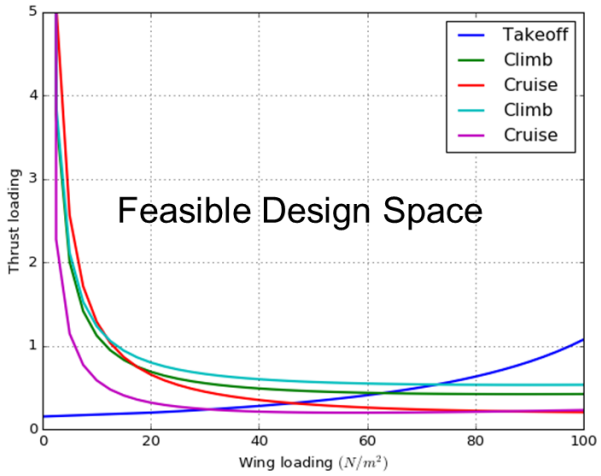

Figure 4. Feasible design space indicated from result of constraint analysis

Once the feasible design space is determined from the constraint equation, it can be used to select different motor, propeller, and battery combinations. The selection of a motor and propeller combination leads to a maximum thrust that can be generated by the propulsion system and therefore an additional constraint represented with a horizontal line in the constraint diagram. Anything above this line requires more thrust that the combination is able to supply and is therefore outside the feasible design space. Figure 5 shows notionally four different motor and propeller combinations, each one represented by a single dotted line. If the line, or a portion of the line, falls within the feasible design space, then a proposed design using this motor and propeller combination may be feasible. Otherwise, no design is feasible with that specific combination. For example, Combo 1 does not have any feasible design because the thrust produced by the combination is insufficient. Combo 2 contains many feasible designs because the motor and propeller can supply enough thrust, enabling designs with wing loadings as low as 16 N/m^2 to as high as 98 N/ m^2, provided the vehicle can be manufactured.

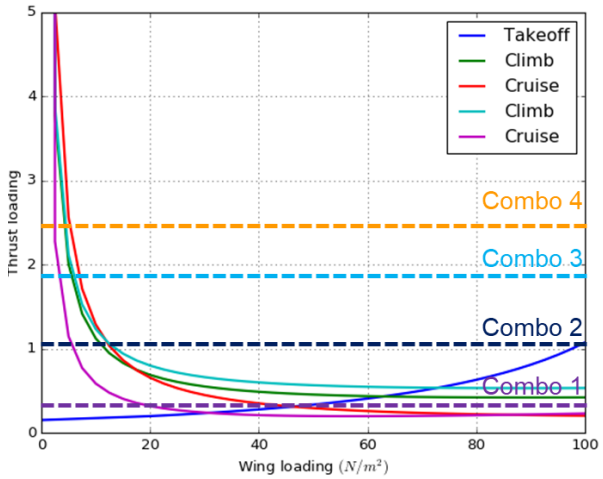

Figure 5. Feasible design space with maximum thrust of motor and propeller combo lines

When feasible designs are possible, several design candidates are selected along the horizontal line representing the thrust loading attained by the Combo and a few are selected along this line for further analyses. A 20% margin on each side (left and right) of the active constraint is retained to ensure sufficient leeway is retained for possible modeling uncertainties (design safety margin). The design candidates for each Combo are represented as yellow dots in Figure 6.

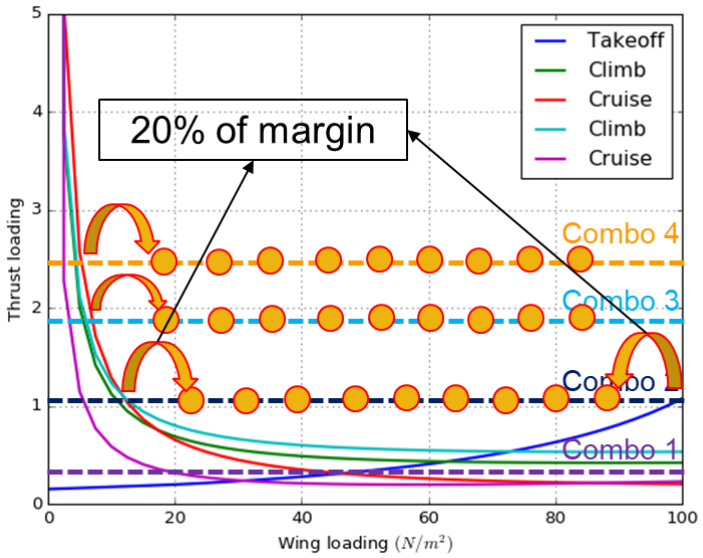

Figure 6. Design point selection using maximum thrust of motor and prop combo

Several sets of wing loading (W_{TO}/S) points are retained from the constraint analysis. From these chosen wing loading values, the takeoff weight for each candidate is computed using the weight estimation procedure laid out in the mission analysis section of this report.

Mission analysis

The mission analysis is performed to calculate the takeoff weight (W_{TO}), which can then be used to determine the wing area (S) from the wing loading (W_{TO}/S). The weight estimation technique starts from the addition of empty weight (W_E) and payload weight (W_P). The payload weight is provided from the mission requirements. The propulsion system weight and the battery weight are pulled from the database of motor and propellers and the database of batteries. The empty weight minus the weight of the installed propulsion systems ($\dot{W_E}$) relative share of the overall vehicle weight is obtained from the designed baseline model. The empty weight calculation depends on the takeoff weight calculation as shown in Equation 2. Therefore, the takeoff weight must be found using a fixed-point iteration method.

$$W_{TO} = W_E + W_P$$

$$W_E = \dot{W}_E + W_{PD} + W_{BAT}$$
$$\dot{W}_E = W_{fuselage} + W_{wing} + W_{tail} + \cdots$$

$$W_E = \dot{\Gamma} W_{TO} + \Phi W_{TO} + \Omega_{BAT} W_{TO}$$

$$Where\ \dot{\Gamma} = \frac{\dot{W}_E}{W_{TO}},\ \Phi = \frac{W_{PD}}{W_{TO}}, \Omega_{BAT} = \frac{W_{BAT}}{W_{TO}}$$
$$W_{TO} = \frac{W_P}{1 - \dot{\Gamma} - \Phi - \Omega_{BAT}}$$

W_{TO}: Takeoff weight
W_E: Empty weight
$\dot{W}_E$: (empty weight) – (propulsion system weight)
W_P: Payload weight
$\dot{\Gamma}$: Empirical empty weight fraction
W_{PD}: Power device weight
W_{BAT}: Battery weight
Φ: Propulsion system weight fraction
Ω_{BAT}: Non-consumable energy storage weight fraction

Equation 2. Weight estimation equation for fixed wing

The previous calculation enables the computation of the energy needed for each mission given a takeoff weight. We adapted the "method of range and endurance estimates" [2] for this step. The adaptation rearranges the minimum required power term to get the energy needed for each mission segment with respect to the takeoff weight. Then the total energy needed for the entire mission is calculated for each battery, and batteries without sufficient energy are discarded. Now, all the feasible design points are on the set of possible thrust loading lines. Once we get a take-off weight estimate, several wing loadings (W_{TO}/S) can be selected and the corresponding wing area (S) can be obtained.

Baseline architecture and drag build up

To obtain meaningful sizing data, drag polar information (induced drag coefficients (K_1 and K_2), and zero-lift drag coefficient (C_{D0})) about the vehicle is needed. To do so, it is necessary to pick a baseline architectures to identify these aerodynamic parameters that should remain fairly constant when the vehicle is scaled up or down. The three fixed wing models from the winning reports of the Design, Build, and Fly competitions were chosen as baseline architectures. These architectures have demonstrated flying capability and were modified slightly to fit the 3D printing manufacturability constraint. Figure 7 shows the modified versions of these three baseline architectures. The first architecture maximizes endurance, the second payload, and the third agility.

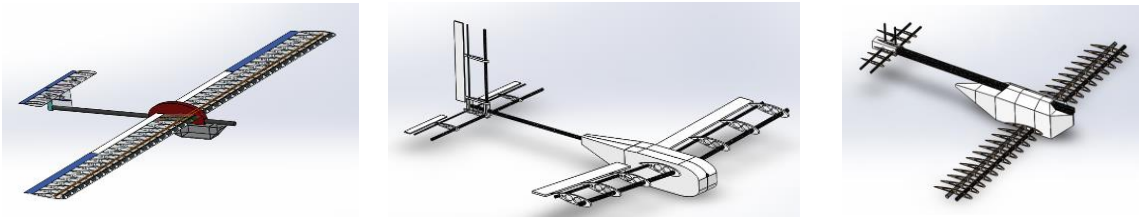

Endurance Agility Payload

Figure 7. Three baseline fixed wing architectures

The drag build-up method was used to estimate their zero-lift drag coefficient. In this method, the drag of all parts of the vehicle (main wing, tail wing, fuselage, motor unit, etc.) is summed together to get an approximate total for the entire vehicle. The obtained zero-lift drag coefficients are used in the constraint analysis outlined above.

Hybrid Vertical Take Off and Landing vehicle

Three baselines architectures capable of Vertical Take Off and Landing were also developed. Each of these architectures was created by adding two booms and four motors to the original three fixed wing baseline architectures. This process is explained graphically in Figure 8, and is inspired from the Arcturus Jump 20 as shown in the rightmost image in Figure 8. A CAD rendition of the three VTOL architectures is shown in Figure 9.

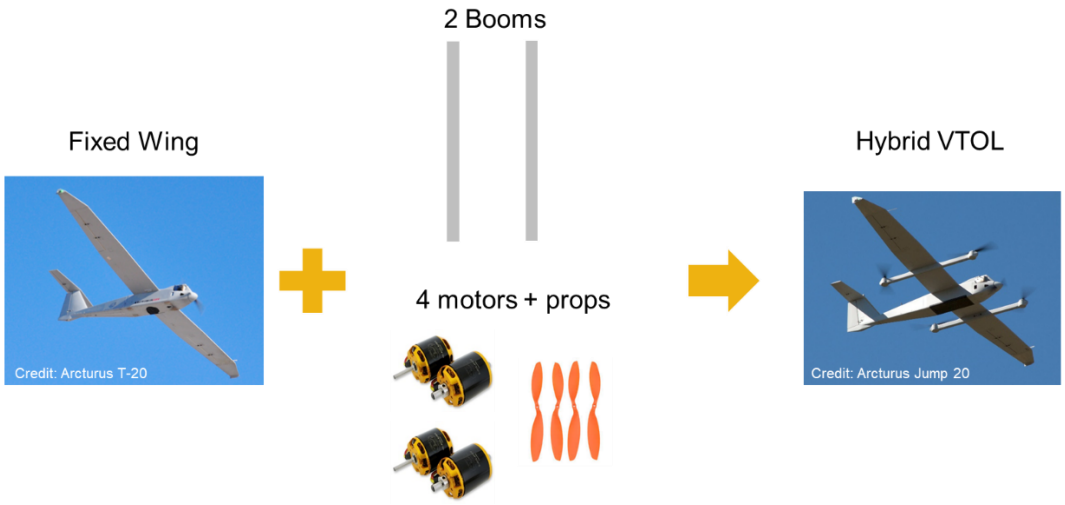

Figure 8. Concept of hybrid VTOL

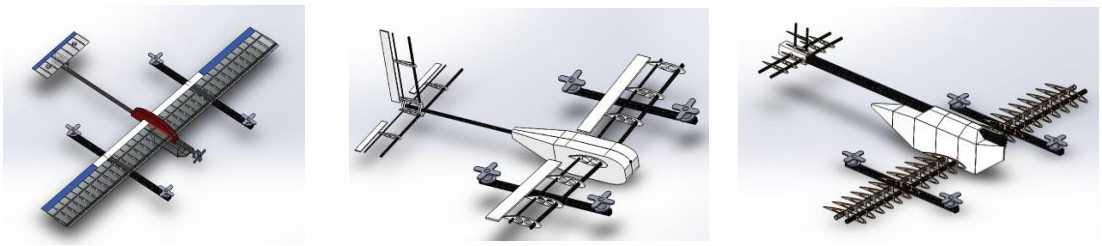

Endurance Agility Payload

Figure 9. Three baseline hybrid VTOL architectures

Constraint analysis

The sizing process for wing area and propulsion system for forward flight for a hybrid VTOL vehicle is identical to the process for of the fixed wing case. However, it is necessary to have updated weight and zero-lift drag coefficients (C_{D0}) due to the additional propulsion systems. The updated zero-lift drag coefficient are shown in Table 1.

Architecture	Wing Area [m^2]	C_{D0} of Fixed Wing	C_{D0} of Hybrid VTOL
1	0.3909	0.0388	0.0558
2	0.0274	0.0508	0.0651
3	0.3401	0.0218	0.0364

Table 1. Zero-lift drag coefficient from drag build up method

Table 1 shows a reasonable increase in C_{D0} for all three hybrid VTOL architectures (relative to their non-VTOL versions). This is expected, as the two additional booms and four additional motors will slightly increase the aerodynamic drag of the vehicle. For hybrid VTOL, the constraint analysis is performed using the same design mission requirements as in the fixed wing case. Additionally, new constraints for the vertical takeoff and vertical landing were considered. Constraints like climb, cruise, and loiter are the same as fixed wing. The feasible design space can be obtained from the constraint analysis as before.

Mission analysis

The mission analysis step for hybrid VTOL is like the analysis performed for the fixed wing architecture, but with a slightly different weight estimation process due to the second propulsion system. Thus, the weight of the second propulsion system denoted W_{PD2} is added in Equation 3. The empty weight minus the weight of installed propulsion systems ($\dot{W_E}$) is also updated for the hybrid VTOL baseline architectures. Another weight analysis for hybrid VTOL is performed with updated equations in order to calculate takeoff weight using a fixed-point iteration method.

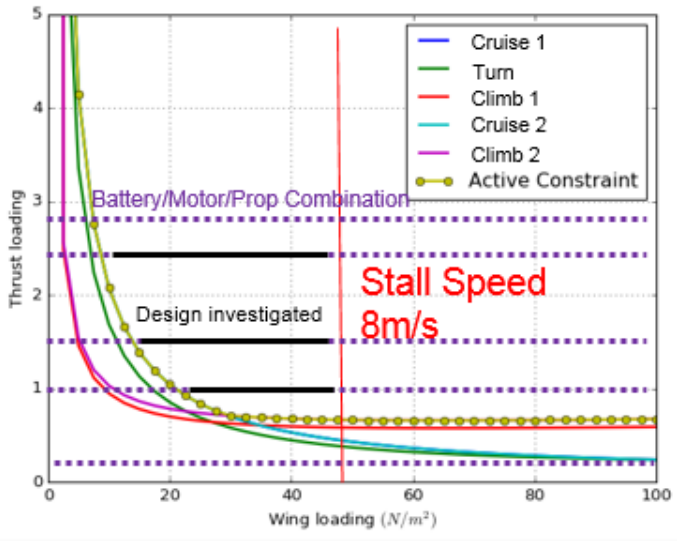

Figure 10: Constraint diagram

$$W_{TO} = W_E + W_P$$

$$W_E = \dot{W}_E + W_{PD1} + W_{PD2} + W_{BAT}$$

$$\dot{W}_E = W_{fuselage} + W_{wing} + W_{tail} + \cdots + W_{Boom}$$

$$W_E = \dot{\Gamma} W_{TO} + \Phi_1 W_{TO} + \Phi_2 W_{TO} + \Omega_{BAT} W_{TO}$$

$$\text{Where } \dot{\Gamma} = \frac{\dot{W}_E}{W_{TO}},\ \Phi_1 = \frac{W_{PD1}}{W_{TO}},\ \Phi_2 = \frac{W_{PD2}}{W_{TO}},\ \Omega_{BAT} = \frac{W_{BAT}}{W_{TO}}$$

$$W_{TO} = \frac{W_P}{1 - \dot{\Gamma} - \Phi_1 - \Phi_2 - \Omega_{BAT}}$$

W_{TO}: Takeoff weight

W_E: Empty weight

$\dot{W}_E$: (Empty weight) – (propulsion system weight)

W_P: Payload weight

$\dot{\Gamma}$: Empirical empty weight fraction

W_{PD1}: Power Device weight 1

W_{PD2}: Power Device weight 2 (VTOL)

W_{BAT}: Battery weight

Φ_1: Propulsion system 1 weight fraction

Φ_2: Propulsion system 2 weight fraction (VTOL)

Ω_{BAT}: Non-consumable energy weight fraction

Equation 3. Weight estimation equation for hybrid VTOL

The energy calculation is also based on the fixed wing energy calculation, but it includes added terms for the vertical takeoff and landing missions. The total energy need for the mission is compared next with the capacity of each battery in the database. Again, batteries with capacities below the energy requirement

are discarded. An additional power constraint for hybrid VTOL vehicle is included in the sizing and synthesis loop to ensure that sufficient power is available to lift the entire vehicle, as shown in Equation 4. A more detailed explanation of these equations is presented in the next section about multicopters where the procedure to estimate the induced velocity is detailed.

$$T_{Climb} = 2\rho A\left(V_C + v_{i,Climb}\right)v_{i,Climb}$$

$$P_{Climb} = T_{climb}\left(V_D + v_{i,Climb}\right)/FOM$$

$$E_{Climb} = P_{climb} \times t_{Climb}$$

$$T_{Descent} = -2\rho A\left(V_D + v_{i,Descent}\right)v_{i,Descent}$$

$$P_{Descent} = T_{Descent}\left(V_D + v_{i,Descent}\right)/FOM$$

$$E_{Descent} = P_{Descent} \times t_{Descent}$$

$v_{i,Climb}$: The induced velocity at the rotor disk in axial climb

$v_{i,Descent}$: The induced velocity at the rotor disk in axial descent

V_C: Rate of climb

V_D: Rate of descent

T_{Climb}: Required thrust in axial climb

$T_{Descent}$: Required thrust in axial descent

P_{Climb}: Required power of axial climb

$P_{Descent}$: Required power of axial descent

E_{Climb}: Required energy of axial climb

$E_{Descent}$: Required energy of axial descent

t_{Climb}: Time to vertical takeoff

$t_{Descent}$: Time to vertical landing

FOM: Figure of merit

Equation 4. Thrust constraint of vertical takeoff and landing

Through this process, a suitable propulsion system for the Power Device 2 of the hybrid vertical takeoff and landing can be selected from the database. The remainder of the design process is identical to that of a fixed wing.

Multicopter vehicle

The ACADIA dashboard features the ability to analyze multicopters in addition to fixed-wing vehicles and hybrid fixed-wing vehicles. Amongst multicopters, the quadcopter functionality has been implemented and the analysis environment can be easily extended to handle hexacopters and octocopters provided the user supply pertinent hexacopter and octocopter information. The multicopter is assumed to be a vehicle architecture featuring a central hub housing the electronics, energy storage, and sensor equipment, as well as several arms supporting the motors and propellers, while acting as landing gears. A computer-aided-design rendition of a quadcopter similar in shape to the quadcopter analyzed in the ACADIA dashboard is presented in Figure 11.

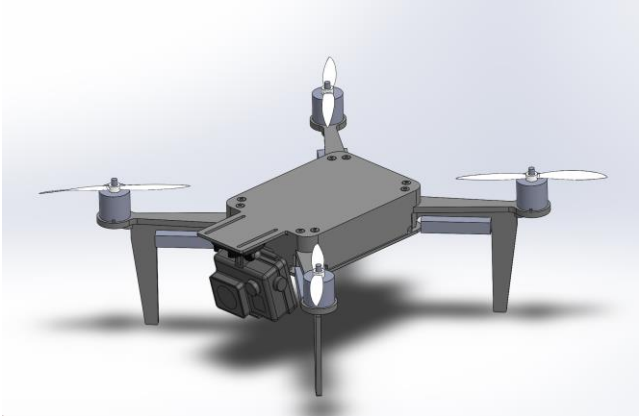

Figure 11: Notional quadcopter model

With the overall design of the multicopter frozen, the next task is to find which combinations of off-the-shelf batteries, motors and propellers allow the multicopter to fly a specific design mission provided by the user. Given the need to fit propellers of different sizes and to ensure that the propellers have sufficient clearance with each other and with the hub, the arms of the multicopter are parametrically adjusted with the diameter of the propellers. Larger propellers require longer arms which increase the overall size of the vehicle (even if the hub remains of the same dimension). This has a direct impact on the drag of the vehicle, on the weight of the vehicle, as well as on the manufacturing time of the vehicle when additive manufacturing technology is used. The vehicle performance must therefore be estimated for each battery, and motor and propeller combination to estimate the amount of power required and the amount of energy needed to fly the design mission.

Mission Analysis

In order to check whether a combination of battery, motor, and propeller mounted on a multicopter structure can successfully fly the design mission, the vehicle performance must be estimated. For a multicopter, this essentially revolves around two questions: 1) Is there enough energy stored and usable in the battery to successfully complete the mission, and 2) Is there enough power available to meet the various payloads, speeds, climbs, and flight altitude requirements. The process used to check these requirements is highlighted in Figure 12

The process starts with a specific combination of motor, propeller and battery. The propeller selection drives the need to resize the multicopter structure. The mass of the multicopter structure is estimated using surrogate models that have been properly fitted beforehand (to be discussed in the vehicle metric section). Next, the overall mass of the vehicle is estimated by adding the mass of the multicopter structure, the mass of the electronic components (radio receiver, GPS antenna, telemetry, switch, wires, speed controllers…), the mass of the payload, the mass of the energy storage (battery), and finally the mass of the propulsion systems (motors and propellers). Subsequently, the design mission is decomposed into multiple legs

(typically takeoff leg, climb leg, cruise leg, loiter leg, descent leg, landing leg) and the energy and power required for each of these legs is estimated. The mission's total energy requirement is then computed by adding the energy contribution of each leg. The mission's maximum power requirement is computed next by comparing the power requirements across all mission legs. This leads to the final step of the analysis which consists in comparing the maximum power required during the mission to the installed power, and in comparing the total mission energy requirement to the usable energy from the battery. If the installed power and energy are greater than the required power and energy, then the design is considered feasible and it is added to the list of feasible designs. Otherwise, the design is not able to satisfy the mission requirements and another combination of motor, propeller, and battery is investigated.

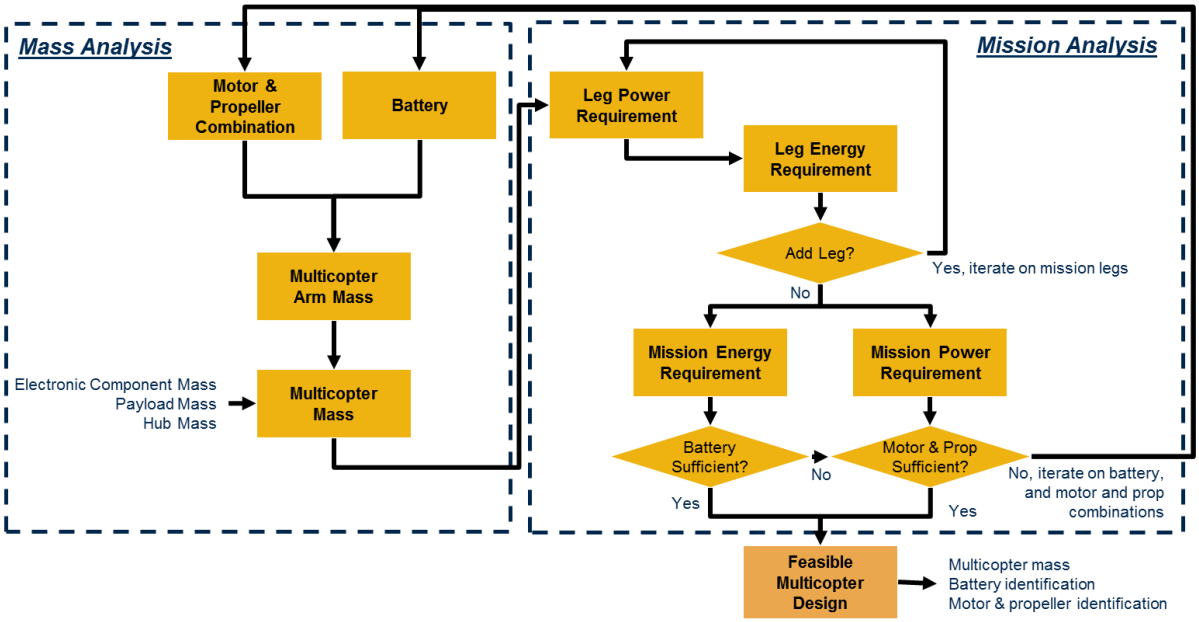

Figure 12: Multicopter Sizing Process

Power Requirements

One question that logically arises is how are the power requirements computed? The process used to estimate power requirements is adapted from traditional helicopter textbooks and follows loosely the methods proposed by Gordon Leishman in *Principles of Helicopter Aerodynamics* [6] and by Raymond Prouty in *Helicopter Performance, Stability and Control* [7]. The notation and parameters used throughout the analysis are described in Figure 13.

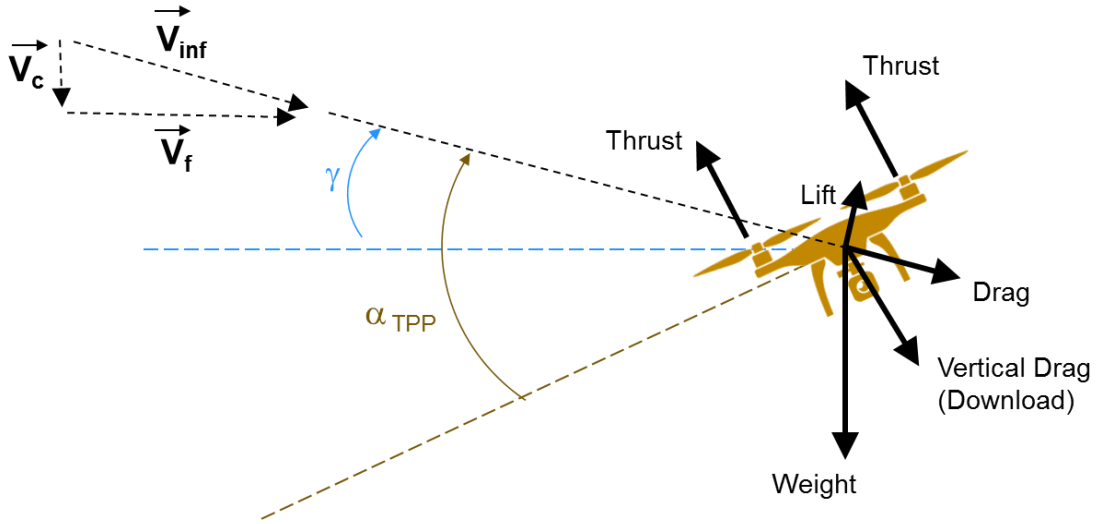

Figure 13: Multicopter Parameter Notation

The essence of the power estimation process is summarized in Figure 14 although some simplifications have taken place to improve the clarity of the figure (i.e. some convergence loops on tip path plane angle of attack, and induced velocity are omitted).

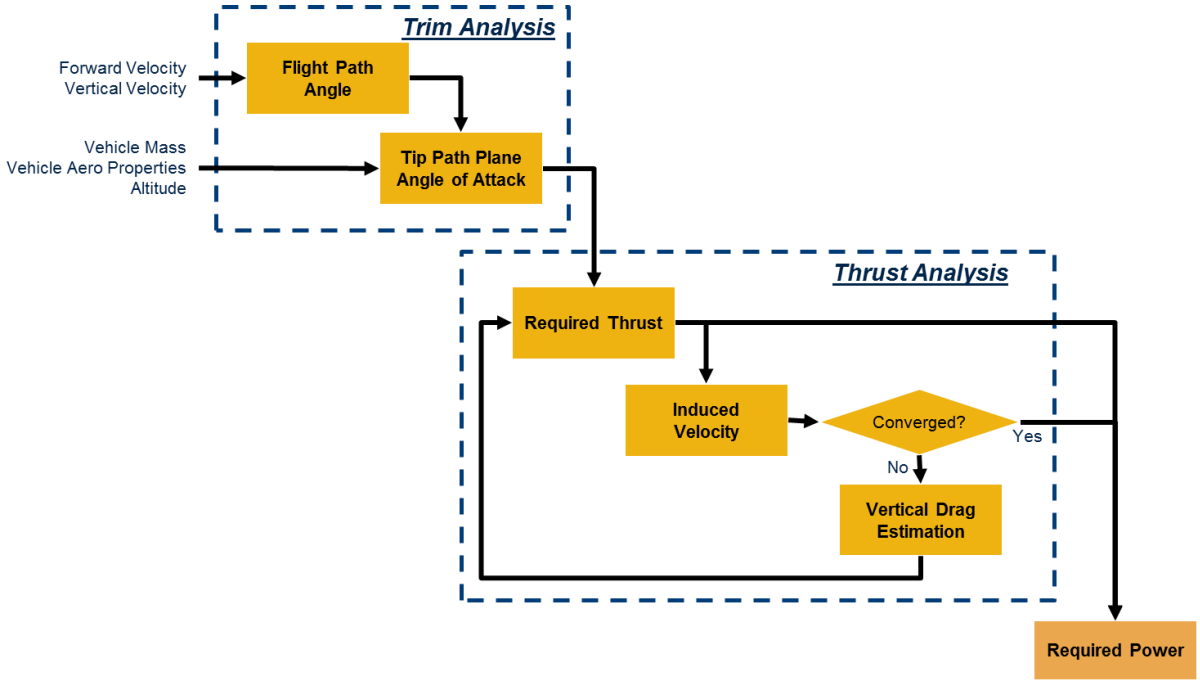

Figure 14: Multicopter power tequirements – (Some details omitted for clarity)

The power requirement computation process starts with an estimation of the flight path angle denoted γ and computed using the rate of climb and the airspeed using Equation 5 below:

$$\gamma = \text{asin}\left(\frac{V_c}{V_\infty}\right) \; with \; V_\infty = \sqrt{V_c^2 + V_f^2}$$

Equation 5: Flight Path Angle

With the flight path angle estimated, the next step is to estimate the tip path plane angle of attack denoted α_{TPP} using the vehicle weight *W*, the multicopter lift *L* and drag *D* due to the free-stream velocity, and the vertical drag due to the induced velocity download on the vehicle structure. The propeller blades are assumed to be rigid and therefore any flapping of the blades is assumed to be negligible. Thus, the tip path plane angle of attack gives an indication of the multicopter attitude when used in conjunction with the flight path angle. The tip path plane angle of attack is computed using the recursive formula in Equation 6 below:

$$\alpha_{TPP} = atan\left(\frac{D + W \cdot sin(\gamma)}{W \cdot \cos(\gamma) - L}\right)$$

Equation 6: Tip Path Plane angle of attack

The drag and the lift produced by the multicopter, when exposed to the free-stream flow, is given by the following equation where f_D and f_L are the equivalent flat plate areas for the drag and lift produced by the multicopter body.

$$D = \frac{1}{2}\rho \cdot f_D \cdot {V_\infty}^2 \; and \; L = \frac{1}{2}\rho \cdot f_L \cdot {V_\infty}^2$$

Equation 7: Multicopter body drag and lift

The estimation of the f_D and f_L parameters is done using experimental wind tunnel tests. Published wind tunnel experimentations with various quadcopter configurations reported in [8] are used to fit a model representing the evolution of f_D and f_L for different vehicle attitudes (tip path planes are assumed to be parallel to hub plan). A quadcopter configuration (*ImpulseRC Alien*) similar in shape to the multicopter architecture being used for this research is retained and a model fit is performed which yields the evolution of the f_D and f_L parameters with α_{TPP}. The reference surface area retained for these estimations is the area between the four electric motors and the curve fits are detailed in Figure 15.

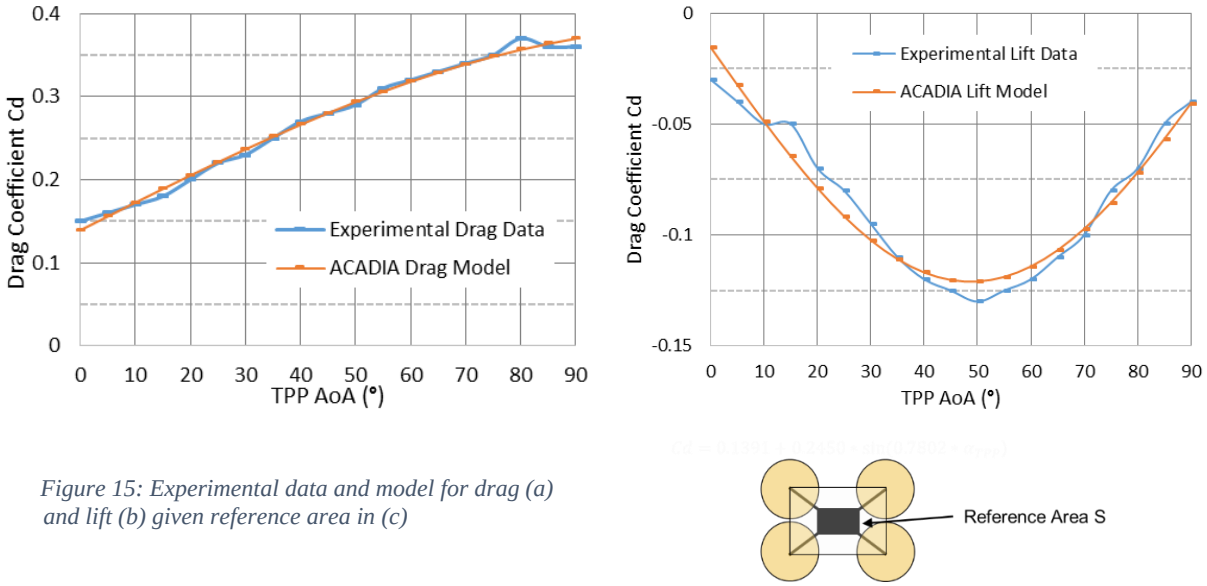

Figure 15: Experimental data and model for drag (a) and lift (b) given reference area in (c)

Concurrently to the tip path plane angle of attack, the thrust required to ensure steady flight (either during cruise, climb, or hover) is estimated accounting for the vertical drag due to the downwash of rotors. It is estimated using the formula below with f_{D_W} being the equivalent flat plate area inside the rotor wake and with *k* a factor being 1 and 2 adjusting the induced velocity speed to its value at the rotor disc (*k=1*) and in the far wake (*k=2*). Currently, the value of *k* is assumed to be 2 as the wake usually contracts over a very short distance. The recursive formula in Equation 8 uses index *i* to indicate the number of iterations reached.

$$T_{i+1} = \left(W\cos(\gamma) - \frac{1}{2}\rho \cdot f_L \cdot {V_\infty}^2\right)^2 + \left(W\sin(\gamma) + \frac{1}{2}\rho \cdot f_D \cdot {V_\infty}^2\right)^2 + \frac{1}{2}\rho \cdot f_{D\_W} \cdot \left(V_C + k * v_{induced_i}\right)^2$$

Equation 8: Thrust required for Multicopters

A further refinement of the thrust model adds the downwash effect or vertical drag effect due to the induced velocity generated to create the thrust, and which impacts the body of the multicopter. To estimate this impact, the value of the induced velocity where it reaches the structure of the quadcopter is required. Far downstream, this velocity is twice the value at the rotor disk. Thus the actual speed of the flow hitting the body of the quadcopter is given using an induced velocity far-wake factor k with value between 1 and 2. Because the flow contracts quickly, it is assumed that this far-wake factor is equal to 2 in this research.

With the thrust estimated, the corresponding induced velocity for each rotor is computed using a recursive formula as shown in the equation below. The thrust for each rotor is assumed to be the vehicle thrust divided by the number of rotors *n* as shown in Equation 9.

$$v_{induced_i} = \frac{T_{i-1}/n}{2\rho \cdot A \cdot \sqrt{(V_\infty \cdot \cos(\alpha_{TPP}))^2 + \left(V_\infty \cdot \sin(\alpha_{TPP}) + v_{induced_{i-1}}\right)^2}}$$

Equation 9: Induced velocity

Several iterations may be required to ensure convergence of the induced velocity, tip path plane angle of attack, and thrust since a change in the induced velocity modifies the vertical drag due to the download on the fuselage, and therefore the thrust required changes.

In axial descent, the simple momentum theory does not hold anymore and thus the induced velocity is computed in two different ways depending on the descent speed. For large rate of descent, an analytical formula is used in the region $V_C/v_h \leq -2$

$$v_{i,Descent} = -\frac{V_D}{2} - \sqrt{\left(\frac{V_D}{2}\right)^2 + v_h^2}$$

For smaller rate of descent, an empirical formulation given by Leishman is used in the region $-2 \leq V_C/v_h \leq 0$

$$v_{i,Descent} = v_h\left(\kappa + k_1\left(\frac{V_D}{v_h}\right) + k_2\left(\frac{V_D}{v_h}\right)^2 + k_3\left(\frac{V_D}{v_h}\right)^3 + k_4\left(\frac{V_D}{v_h}\right)^4\right)$$

With $\kappa = 1.15, k_1 = -1.125, k_2 = -1.372, k_3 = -1.718, and\ k_4 = -0.655$

Once this 'outer loop' has converged to the trimmed solution, the required power is computed using the thrust estimate as well as the free-stream airspeed and the induced velocity as shown in Equation 10 below. It uses the figure of merit of the rotor, *FOM*, which is assumed to be 0.40 for the small rotors under investigation.

$$P_{req} = \frac{n \cdot T \cdot (V_\infty \cdot \sin(\alpha_{TPP}) + v_{induced})}{FOM}$$

Equation 10: Power required for multicopter

IV. Vehicle Performance and Capability Metrics

The sizing and synthesis analysis yields a list of vehicles able to meet the requirements of the design mission. These vehicles are designed by combining pre-existing components that are available off-the-shelf and that are representative of the inventory of components that could be forward deployed in support of soldiers in operations. Because the vehicles use off-the-shelf components, their capabilities might exceed, sometimes substantially, the requirements of the design mission. These capabilities exist because the feasible vehicle designs are overbuilt owing to the discrete nature of the performance space for the major components.

In order to compare the extra capabilities provided by the different architectures, some metrics of interest are selected for further evaluation of the vehicles. In turn, this yields additional information regarding the true capabilities and shortcomings of the different architectures under review. This can be useful to document realistic sets of requirements for future small unmanned aerial systems. The metrics retained can be classified into two categories, performance metrics and ease-of-deployment metrics. Among the performance metrics, maximum range, maximum endurance, maximum altitude, maximum rate-of-climb are selected. Among the ease-of-deployment metrics, manufacturing time and packing volume are selected.

Maximum endurance and Maximum range

Fixed Wing and Hybrid VTOL vehicles

Maximum endurance and maximum range of an aircraft describes the maximum duration or the maximum distance the vehicle can fly. The main assumption behind the formulation of the maximum endurance and maximum range analytical equation is the usable capacity of the battery which is typically a function of the discharge current and the temperature. In this analysis the dependency on temperature is not accounted for and the discharge current is assumed to be constant over time. The discharge time *t* is computed using the Peukert's equation, listed in Equation 11.

$$\mathrm{t} = \frac{C}{i^n}$$

Equation 11: Peukert's equation

Then, from the aerodynamic assumptions listed in Equation 12, the equations for the maximum endurance and range can be derived as seen in Equation 13. More details on this derivation are listed in reference [5]. In the maximum endurance and maximum range equations, *Rt* denotes the battery hour rating (in hours). In Equation 13 and Equation 14, the air density is computed using the design mission cruising altitude.

Maximum Endurance: $C_{D0} = \frac{1}{3} k C_L^2$

Maximum Range: $C_{D0} = k C_L^2$

Equation 12: Aerodynamic assumptions for maximum endurance and range

$$E_{max} = Rt^{1-n} \left(\frac{\eta_{tot} V \times C}{(2/\sqrt{\rho S}) C_{D0}^{1/4} (2W\sqrt{k/3})^{3/2}} \right)^n h$$

Equation 13: Maximum endurance calculation for battery powered aircraft

The maximum range is calculated by multiplying maximum endurance by the flight velocity for maximum range, computed from the aerodynamic assumption listed above. The resulting equation is shown in Equation 14.

$$R_{max} = Rt^{1-n} \left(\frac{\eta_{tot} V \times C}{(2/\sqrt{\rho S}) C_{D0}^{1/4} (2W\sqrt{k})^{3/2}} \right)^n \sqrt{\frac{2W}{\rho S} \sqrt{\frac{k}{C_{D0}}}} 3.6$$

Equation 14: Maximum range calculation for battery powered aircraft

Multicopter vehicles

The maximum endurance and maximum range speeds do not have a closed-form solution and are therefore estimated using the power requirement curve representing the power required to sustain level and steady flight at different forward speeds. The best endurance speed is the speed for which the power requirement is the lowest. The best range speed is the speed for which the ratio power-over-speed is the lowest (shallowest line going the origin to any point in the power required curve). The maximum speed is the speed at which the power required curve crosses the installed power curve. This is explained in Figure 16 which showcases the power requirement curve for the 5 inch quadcopter that was test flown during the AEWE 2017 exercise. In this specific case, the best endurance speed is 14m/s, the best range speed is 18m/s and the maximum speed is 24m/s.

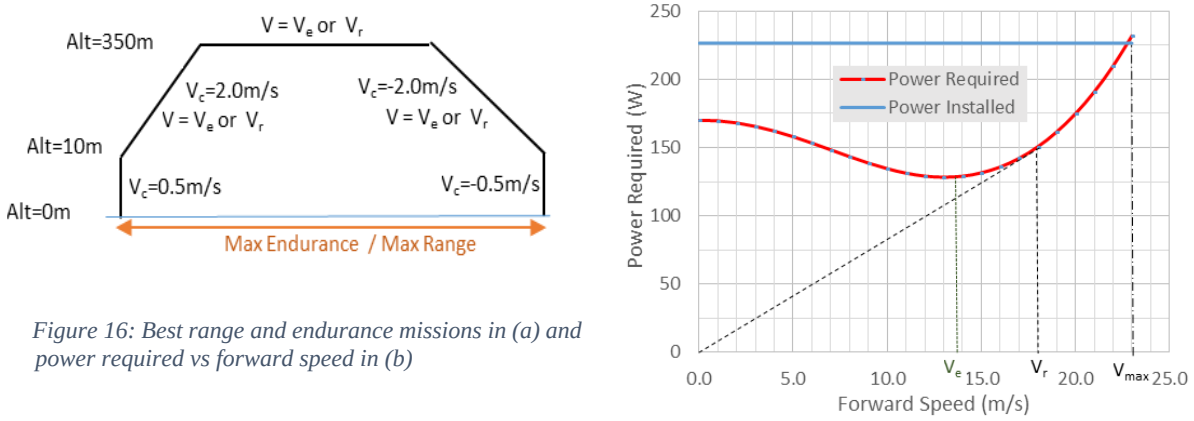

Figure 16: Best range and endurance missions in (a) and power required vs forward speed in (b)

The maximum endurance is then computed by dividing the battery usable energy capacity by the power required in forward flight at the best endurance speed after removing energy allowances for takeoff and landing. This leads to a maximum endurance of 1421 seconds (23 minutes and 41 seconds) for the 5" quadcopter used during the AEWE experiment.

The maximum range is then computed by dividing the battery usable energy capacity by the power required in forward flight at the best range speed after removing energy allowances for takeoff and landing. This leads to a maximum range of 21,566 meters (21km) for the 5" quadcopter used during the AEWE experiment.

Maximum altitude – Absolute ceiling

Fixed Wing and Hybrid VTOL vehicles

Absolute ceiling describes how high an airplane can fly in steady, level flight. Absolute ceiling is defined as the altitude where the maximum rate of climb is 0 ft/min. Analytical estimation of absolute ceiling for fixed wing vehicle can be calculated using Equation 15 from Anderson.

$$\frac{\eta_{pr}P}{W} = \left[\frac{2}{\rho_\infty}\sqrt{\frac{K}{3C_{D,0}}}\left(\frac{W}{S}\right)\right]^{1/2}\frac{1.155}{\left(\frac{L}{D}\right)_{max}}$$

Equation 15: Fixed Wing and Hybrid VTOL Maximum Altitude

Multicopter vehicles

The maximum altitude is determined by the altitude at which the power installed matches the power required in some specific flight configuration. For this analysis, the maximum altitude is taken in hover conditions. Incidentally, this also means that this may not be the absolute maximum rate of climb that the multicopter is able to achieve as this would be achieved in forward flight when power requirements are less, probably at an airspeed close to the best range speed. A bisection algorithm is used to search for the altitude at which this condition occurs.

Maximum rate of climb

Fixed Wing and Hybrid VTOL vehicles

The maximum sea-level rate of climb for a fixed wing and hybrid VTOL vehicle is determined by the excess power, namely the difference between the installed power and the required power in some specific flight configuration. The expression in Equation 16 is used to determine the maximum rate of climb.

$$ROC_{MAX} = \frac{\eta_{pr} P}{W} - \left[\frac{2}{\rho_\infty}\sqrt{\frac{K}{3C_{D,0}}}\left(\frac{W}{S}\right)\right]^{1/2} \frac{1.155}{\left(\frac{L}{D}\right)_{max}}$$

Equation 16: Fixed Wing and Hybrid VTOL Maximum Rate Of Climb

Multicopter vehicles

The maximum sea-level rate of climb for a multicopter is determined by its excess power, namely the difference between the installed power and the required power in some specific flight configuration. For this analysis, the rate of climb is taken in vertical flight conditions which means that it is defined using the excess power in hover. Incidentally, this also means that this may not be the absolute maximum rate of climb that the multicopter is able to achieve as this would be achieved in forward flight when power requirements are less, probably at an airspeed close to the best range speed. The maximum rate of climb in vertical flight is given by the expression below:

$$ROC_{MAX} = 2 \cdot v_{induced}^{Hover} \cdot \left(\frac{P_{installed}}{P_{req}^{Hover}} - 1\right)$$

Equation 17: Multicopter Maximum Rate of Climb

Mechanical complexity

The mechanical complexity metric stems from the intent to capture and compare the reliability of the different architectures. Unfortunately, reliability is a difficult metric to predict without proper testing of the different components and in particular without performing accelerated testing. As a result, a simpler metric is retained and the number of parts making up the vehicle design is selected as a proxy for the complexity and reliability of the entire system.

Fixed Wing vehicles

For fixed wing vehicles, as the vehicle is scaled, the numbers of ribs in the main wing and in the empennage are also scaled. Note that in fixed wing vehicle, the numbers of ribs are set to zero since it varies with the scaled wing area. The number of fixed parts in the fixed wing vehicle is 128 as highlighted in Table 2. The number of ribs can be calculated by dividing the wing span by 2.5. The value of 2.5 inches corresponds to the spacing between ribs and was obtained by looking into typical spacing used in the hobbyist community and from experience. For the main wing and the horizontal tail, since the number of ribs should be evenly distributed between the two sides, the number of ribs are floored to the nearest even number.

Table 2: Fixed wing vehicle complexity

	Electronic			Structural			Mechanical / Servos		
Assembly	**Item No.**	**Part Name**	**Amount**	**Item No.**	**Part Name**	**Amount**	**Item No.**	**Part Name**	**Amount**
Horizontal Stabilizer	1	Servo	1	3	Ribs	0	10	Push Rod	1
	2	Servo wire	1	4	Rudder	1	11	Servo Horn	1
				5	Hinge	1	12	Servo Horn screw	1
				6	Hinge Screw	4	13	Servo mount screws	2
				7	Spar	2	14	Control Horn	1
				8	I-beam shear web	1	15	Control Horn Screws	4
				9	Laminating Film	1			
Vertical Stabilizer	1	Servo	1	3	Ribs	0	9	Push Rod	1
	2	Servo wire	1	4	Rudder	1	10	Servo Horn	1
				5	Hinge	1	11	Servo Horn screw	1
				6	Hinge Screw	4	12	Servo mount screws	2
				7	Spar	2	13	Control Horn	1
				8	Laminating Film	1	14	Control Horn Screws	4
Main Wing	1	Servo	2	3	Ribs	0	10	Push Rod	2
	2	Y-adaptor servo wire	1	4	Spar	2	11	Servo Horn	2
				5	I-beam shear web	2	12	Servo Horn screw	2
				6	Aileron	2	13	Servo mount screws	4
				7	Laminating Film	2	14	Control Horn	2
				8	Hinge for Aileron	2	15	Control Horn Screws	8
				9	Hinge Screw	8			
Tower (Main Electronic)	1	Radio Receiver	1	15	Tower Structure	1	17	Screw	14
	2	PPM encoder	1	16	Main Wing Torsion Connector	2			
	3	Encoder wire unit	1						
	4	BEC	1						
	5	Speed Controller	1						
	6	Battery	1						
	6	Telemetry	1						
	7	Telemetry wire	1						
	8	GPS	1						
	9	GPS wire	1						
	10	Power Module	1						
	11	Power wire	1						
	12	Screammer	1						
	13	Buzzer	1						
	14	Safety switch	1						
Motor Unit	1	Motor	4	3	Motor mount	1	5	Propeller	1
	2	ESC	1	4	Motor mount screws	4	6	Propeller adapter	1
Total			**27**			**45**			**56**
								Grand Total	**128**

Hybrid VTOL vehicle

For hybrid-VTOL vehicles, as the vehicle is scaled, the numbers of ribs in the main wing and in the empennage are also scaled. The number of fixed parts in the hybrid VTOL is 173 as shown in Table 3. Like the fixed wing vehicle, the number of ribs can be calculated by dividing the wing span by 2.5.

Table 3: Hybrid VTOL vehicle complexity

3	Electronic			Structural			Mechanical / Servos		
Assembly	**Item No.**	**Part Name**	**Amount**	**Item No.**	**Part Name**	**Amount**	**Item No.**	**Part Name**	**Amount**
Horizontal Stabilizer	1	Servo	1	3	Ribs	0	10	Push Rod	1
	2	Servo wire	1	4	Rudder	1	11	Servo Horn	1
				5	Hinge	1	12	Servo Horn screw	1
				6	Hinge Screw	4	13	Servo mount screws	2
				7	Spar	2	14	Control Horn	1
				8	I-beam shear web	1	15	Control Horn Screws	4
				9	Laminating Film	1			
Vertical Stabilizer	1	Servo	1	3	Ribs	0	9	Push Rod	1
	2	Servo wire	1	4	Rudder	1	10	Servo Horn	1
				5	Hinge	1	11	Servo Horn screw	1
				6	Hinge Screw	4	12	Servo mount screws	2
				7	Spar	2	13	Control Horn	1
				8	Laminating Film	1	14	Control Horn Screws	4
Main Wing	1	Servo	2	3	Ribs	0	10	Push Rod	2
	2	Y-adaptor servo wire	1	4	Spar	2	11	Servo Horn	2
				5	I-beam shear web	2	12	Servo Horn screw	2
				6	Aileron	2	13	Servo mount screws	4
				7	Laminating Film	2	14	Control Horn	2
				8	Hinge for Aileron	2	15	Control Horn Screws	8
				9	Hinge Screw	8			
Tower (Main Electronic)	1	Radio Receiver	1	15	Tower Structure	1	17	Screw	14
	2	PPM encoder	1	16	Main Wing Torsion Connector	2			
	3	Encoder wire unit	1						
	4	BEC	1						
	5	Speed Controller	1						
	6	Battery	1						
	6	Telemetry	1						
	7	Telemetry wire	1						
	8	GPS	1						
	9	GPS wire	1						
	10	Power Module	1						
	11	Power wire	1						
	12	Screammer	1						
	13	Buzzer	1						
	14	Safety switch	1						
Motor Unit	1	Motor	4	3	Motor mount	1	5	Propeller	1
	2	ESC	1	4	Motor mount screws	4	6	Propeller adapter	1
VTOL Mechanism	1	Motor	4	6	Motor mount	4	10	Propeller	4
	2	ESC	4	7	Motor mount screw(1 set: 3)	12	11	Propeller adapter	4
	3	Power wire	1	8	Boom	2			
	4	Power module	1	9	Boom Screws bolts and nuts	8			
	5	Battery	1						
Total			**38**			**71**			**64**
								Grand Total	**173**

Quadcopter vehicles

For quadcopters, the number of parts does not change as the same number parts are simply scaled up or down to meet the mission requirements. The results are shown in Table 4. For more complex multicopters such as hexacopters and muticopters, the number of parts would be increased however.

Table 4: Quadcopter vehicle complexity

	Electronic			Structural			Mechanical /Servos		
Assembly	**Item No.**	**Part Name**	**Part #**	**Item No.**	**Part Name**	**Part #**	**Item No.**	**Part Name**	**Part #**
Tower (Main Electronic)	1	Radio Receiver	1	15	Hub Structure	2	18	Part screw	14
	2	PPM encoder	1	16	Arms	4			
	3	Encoder wire unit	1	17	Arm bolts	8			
	4	BEC	1	18	Arm nuts	8			
	5	Speed Controller	1						
	6	Battery	1						
	6	Telemetry	1						
	7	Telemetry wire	1						
	8	GPS	1						
	9	GPS wire	1						
	10	Power Module	1						
	11	Power wire	1						
	12	Screammer	1						
	13	Buzzer	1						
	14	Safety switch	1						
Motor Unit	1	Motor	4	3	Motor mount screws	16	5	Propeller	4
	2	ESC	4	4	Motor cap	4	6	Propeller cone	4
					Motor washer	4			
Total			**23**			**46**			**22**
								Grand Total	**91**

Packability

The packability of the different classes of vehicles under review is calculated based on the multiplication of maximum height, width, and length in the vehicle's packed configuration. The result is the volume of a rectangular box.

Fixed Wing Vehicles and Hybrid VTOL vehicles

For the fixed wing and the hybrid VTOL vehicles, there are three baseline vehicles: Endurance driven, Agility driven, and Payload driven. Packability of the three fixed wing vehicles are calculated by detaching the wings and placing them beside the fuselage as shown in Figure 17. In the case of hybrid VTOL

vehicles, since it is a copy of the fixed wing model with two extra booms and four extra motor holders, the packing volume is assumed to be identical between regular and the VTOL variant.

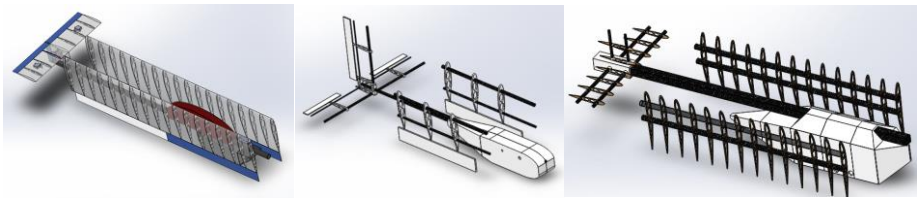

Figure 17: Packing volume layout of the different fixed wing and hybrid VTOL architectures

The logic behind the calculation of the packing volume relies on the estimation of the height, width, and length of the volume occupied by the vehicle once prepared for transportation as shown in Figure 18 which depicts the vehicle viewed from the front. The two sections of the wing are assumed to be placed 5 inches away from the center of the fuselage for endurance driven and agility driven vehicle when packing. For payload driven vehicle, the wing is assumed to be about 6 inches from the center of the fuselage owing to the larger fuselage.

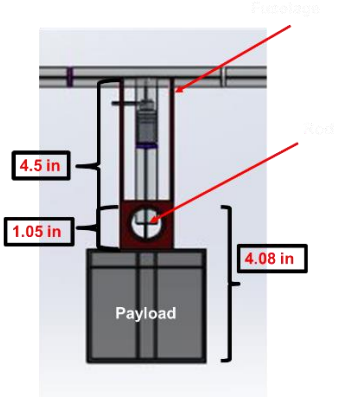

Height:
If VT span/2+4.08 is < Wing Chord
Height = Wing Chord
Else
Height = VT span/2+4.08

Width:
If 5 < HT span/2
Width = HT span
Else
Width = 8

Length:
If Fuselage length + VT Chord/5 < Wing span/2+VT Chord
Length = Wing span/2+VT Chord
Else
Length = Fuselage length + VT Chord/5

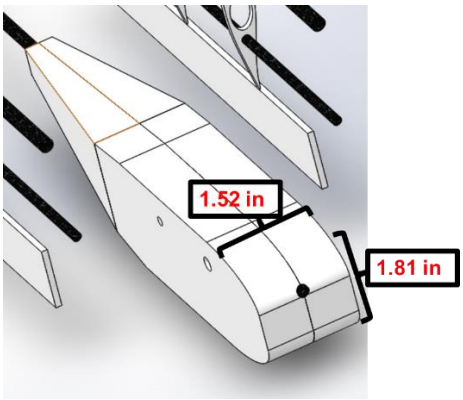

Height:
If VT span/2+(1.81/2) is < Wing Chord
Height = Wing Chord
Else
Height = VT span/2+(1.81/2)

Width:
If 5 < HT span/2
Width = HT span
Else
Width = 10

Length:
If Fuselage length + VT Chord/5 < Wing span/2+VT Chord
Length = Wing span/2+VT Chord
Else
Length = Fuselage length + VT Chord/5

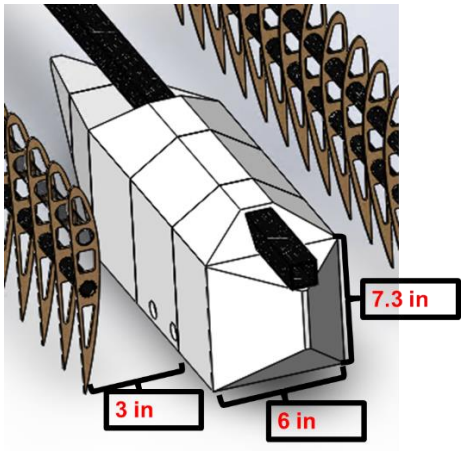

Height:
If VT span/2+7.3 is < Wing Chord
Height = Wing Chord
Else
Height = VT span/2+7.3

Width:
If (6+3+3) < HT span
Width = HT span
Else
Width = 12

Length:
If Fuselage length – HT Chord < Wing Span/2
Length = Wing Span/2
Else
Length = Fuselage length – HT Chord

Figure 18: Packing volume and logic behind the maximum height, width, and length calculation

Quadcopter Vehicles

For quadcopter vehicles, packability is calculated by multiplying the height of the vehicle by the ground footprint, assuming that the propellers and have been removed as shown in Figure 19.

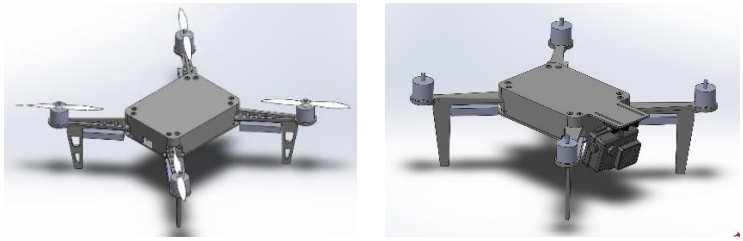

Figure 19: Quadcopter in flying and packed configuration

Vehicle Mass

For weight calculation of the proposed design, CAD volume from different class of vehicles is multiplied by an estimated density of the material. Since the vehicles are being scaled, the volume of the vehicle changes with the scaling variable and therefore the weight.

Fixed Wing Vehicles and Hybrid VTOL vehicles

For fixed wing and VTOL vehicles, the scaling variable is the main wing area. The number of ribs, length of the fuselage, and size of spars are all dependent on the main wing area. The fuselage and the payload bay is kept at the same size as the baseline vehicle throughout the scale change. To predict the volume of the given class of fixed wing vehicle, the volume of the vehicle from CAD is recorded and

fitted/estimated with a polynomial equation. Particularly, most of the results are fitted with a second order response surface equation as shown in Equation 18. All regression was conducted in JMP.

$$R = b_0 + \sum_{i=1}^{k} b_i x_i + \sum_{i=1}^{k} b_{ii} {x_i}^2 + \sum_{i=1}^{k-1} \sum_{j=i+1}^{k} b_{ij} x_i x_j + \varepsilon$$

Equation 18: Response surface equation

The regression for endurance fixed wing and VTOL are shown below. The corresponding equations are incorporated into the current code, but not explicitly displayed in this report. In the regression models, notice the R^2 value and the scattering pattern for residuals. Also note the change in model fit error (MFE) and the model representation error (MRE). MFE shows the error between the data used to fit the model and the model. MRE shows the error between data not used to fit the model and the model. Therefore, with a relatively good fit, the standard deviation between the MFE and MRE should not change much. For each data, 70% of the data points are used for training and 30% is used for Validation.

Endurance driven vehicle volume regression

This volume data is fit with a third order polynomial with wing area as the independent variable is shown in Figure 20. Notice the R^2 value of 1 and the small change in standard deviation change of MFE and MRE.

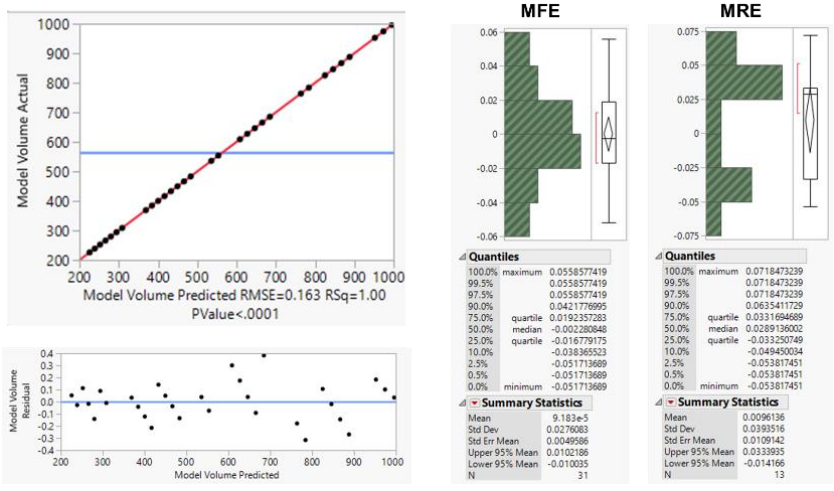

Figure 20: Endurance driven vehicle volume regression

Endurance driven VTOL vehicle volume regression

The volume of the endurance VTOL model was found from taking the volume of the endurance model with addition of booms and motor holders as shown in Figure 21. Again, the data is fitted with a third order polynomial.

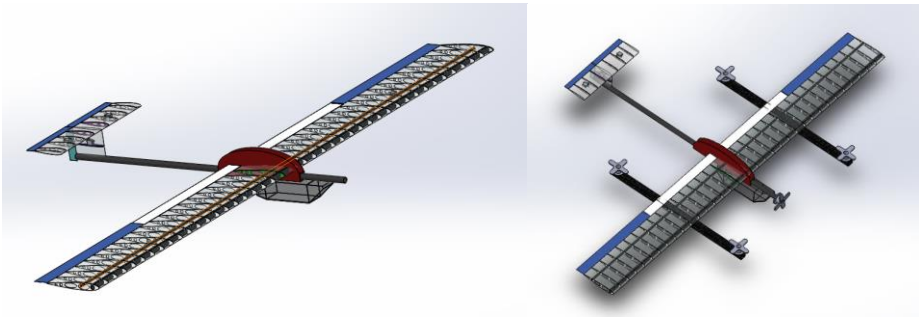

Figure 21: Change to VTOL vehicle of endurance driven vehicle

The result from the regression is shown in Figure 22. Again, note the small change of standard deviation between MFE and MRE.

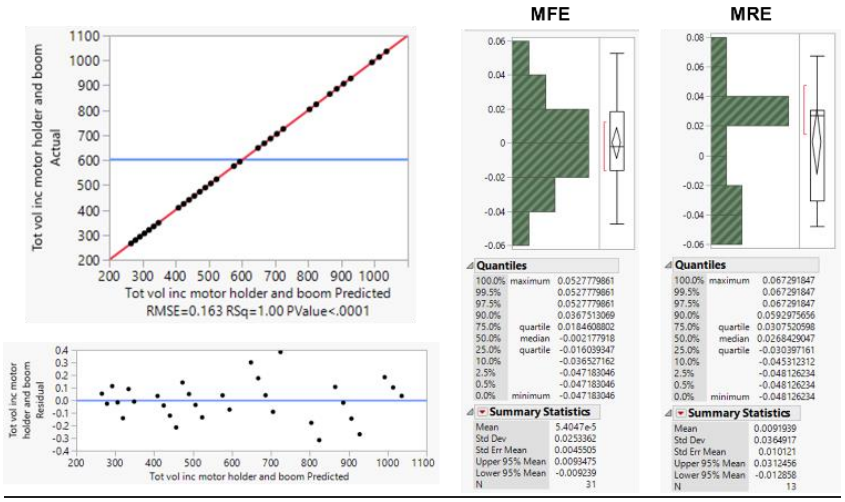

Figure 22: Endurance driven VTOL volume regression

Agility driven vehicle volume regression

For the agility driven vehicle, a second order response surface equation is fitted. Notice the resulting R^2 of 0.99 and the small standard deviation change. Although there seems to be some pattern in the residual, the values are small compared to the predicted values.

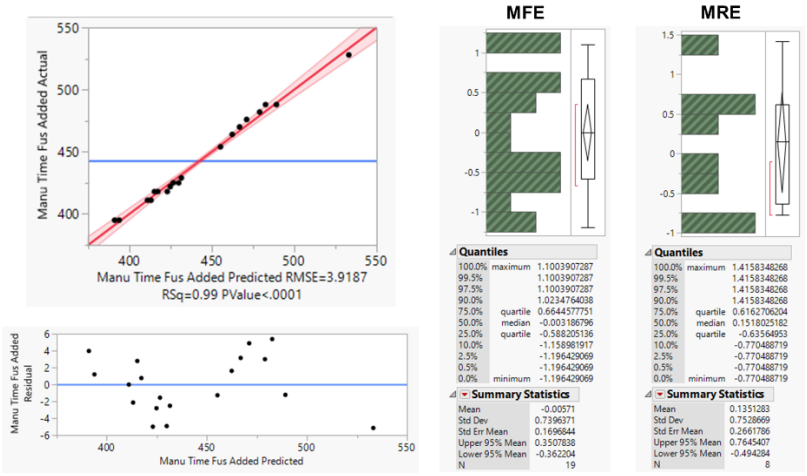

Figure 23: Agility driven volume regression

Agility driven VTOL vehicle volume regression

Similar to the endurance driven VTOL vehicle, the only difference between fixed wing and VTOL are the additional booms and the motors.

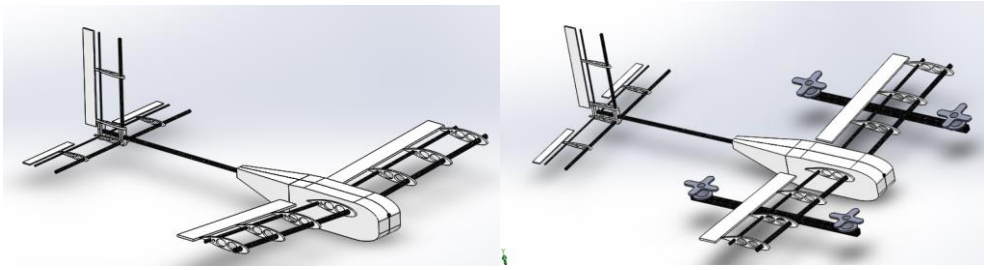

Figure 24: Change to VTOL vehicle of agility driven vehicle

Again, notice the small standard deviation change and the R^2 of 1.

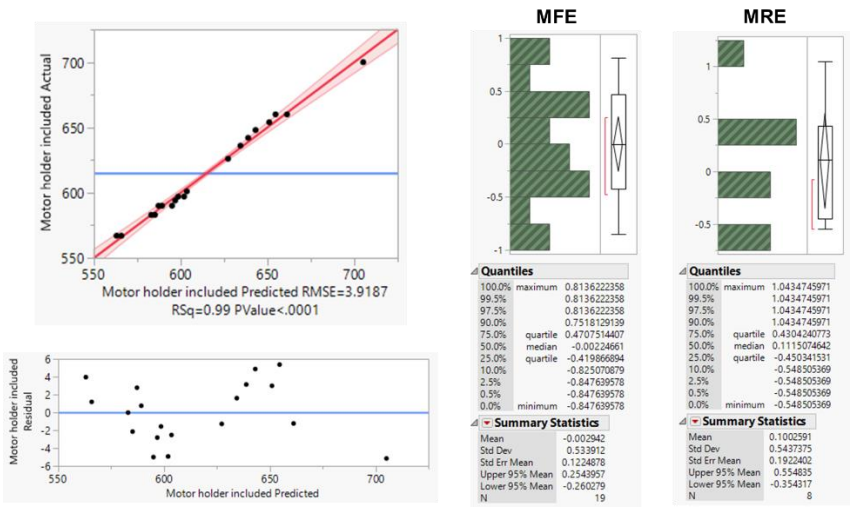

Figure 25: Agility driven VTOL vehicle volume regression

Payload driven vehicle volume regression

The payload driven vehicle volume regression is shown in Figure 26.

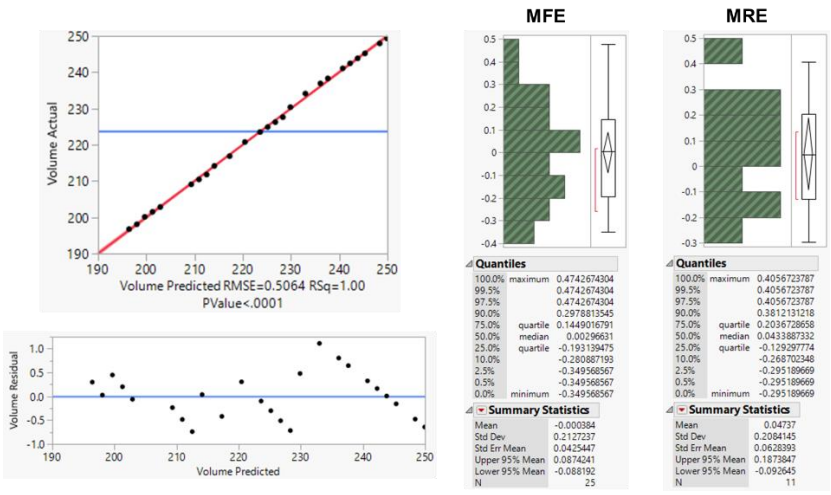

Figure 26: Payload driven vehicle volume regression

Payload driven VTOL vehicle volume regression

Similar to other fixed wing designs, the VTOL vehicle adds the booms and the motor holders to the baseline design.

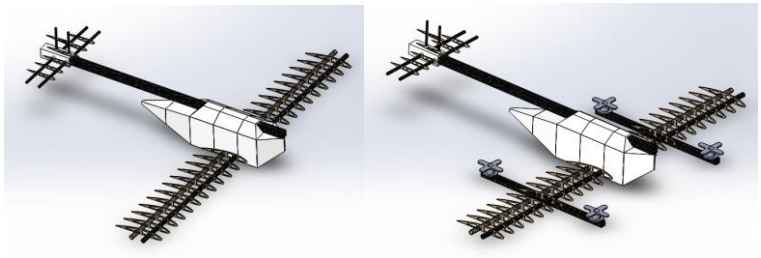

Figure 27: Change to VTOL vehicle of payload driven vehicle

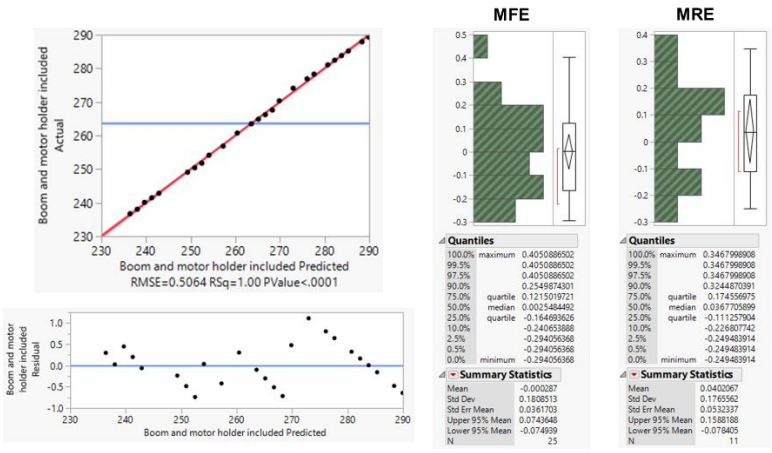

Figure 28: Payload driven VTOL vehicle volume regression

Note the small change in standard deviation between MFE and MRE and the R^2 value of 1. From the volume regression equations for different class of vehicles, the estimated weight can be found by multiplying the estimated volume by the density of the material. Because this is an estimation, a constant density can be assumed for the entire model.

Manufacturing time

For the calculation of manufacturing time, a similar method to the volume regression is followed. The 3D printer currently available for this research is *Stratasys uPrint SE*. The software required to run this printer is called Catalyst EX. Catalyst EX generates an estimated print time with a given STL file.

Fixed wing vehicle

For the fixed wing vehicle, the parts that was assumed to be 3D printed for regression are the ribs, fuselage, and the payload bay. The fuselage and payload bay are denoted in Figure 29.

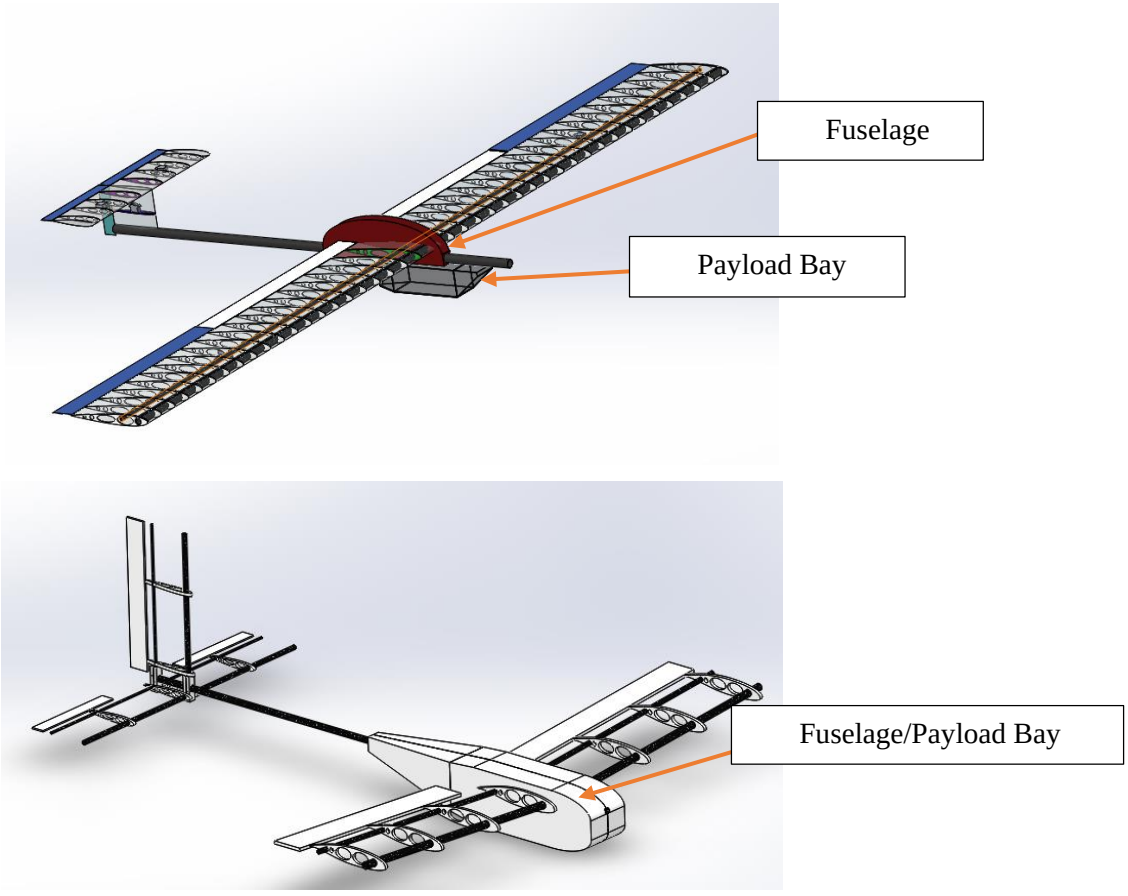

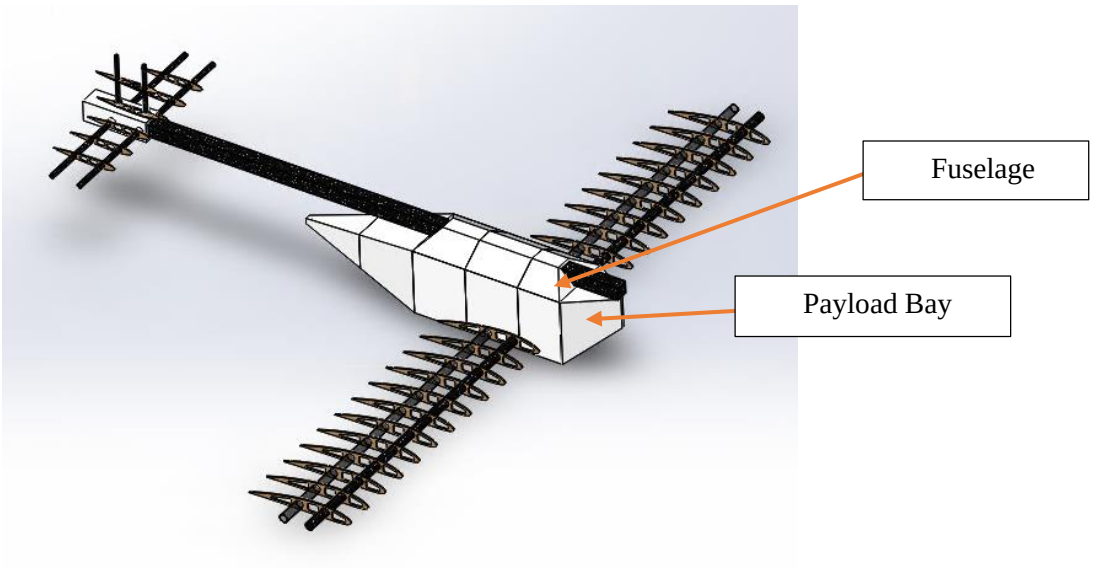

Figure 29: Fuselage and the payload bay locations in three baseline fixed wing vehicles

Endurance driven vehicle manufacturing time regression

The manufacturing time of the endurance model was fitted with a second order model. As with the volume regressions, notice the R^2 value of 1, scattering of the residuals, and the small change of standard deviation between MFE and MRE in Figure 30.

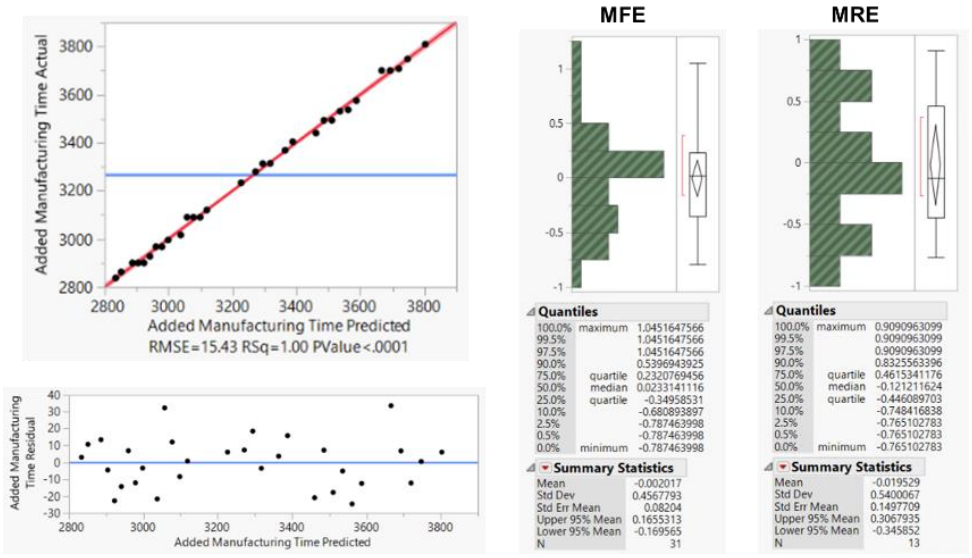

Figure 30: Endurance driven vehicle manufacturing time regression

Endurance driven hybrid VTOL vehicle manufacturing time regression

The change to VTOL adds the additional time from printing the four motor holders as shown in Figure 21. Note that an addition of constant value does not change the regression result by much as highlighted in Figure 31.

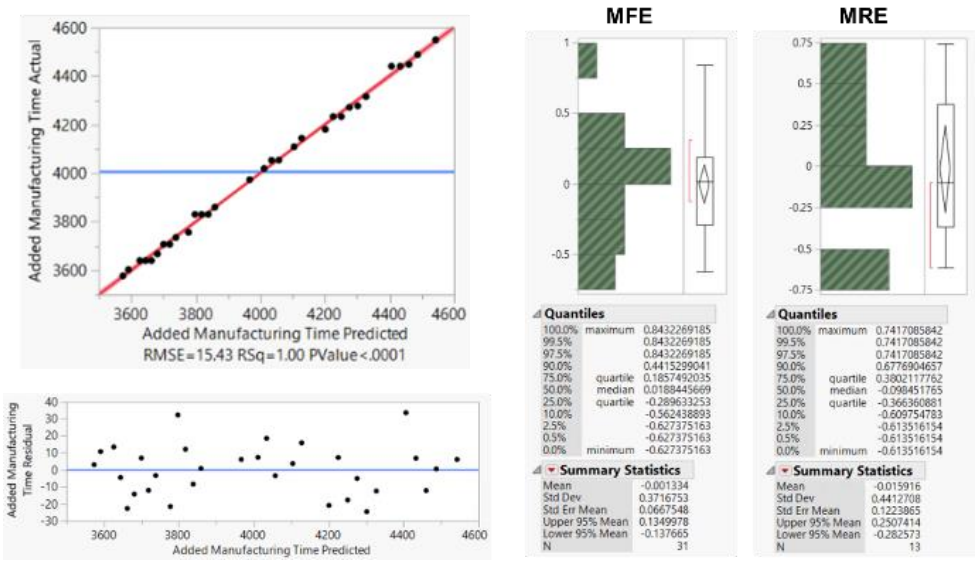

Figure 31: Endurance driven VTOL vehicle manufacturing time regression

Agility driven fixed wing vehicle manufacturing time regression

The manufacturing time for agility driven vehicle is fitted with a second order model based on wing area as independent variable. In Figure 32, the residuals show a little pattern, but since they are small compared to the predicted value, the resulting fitted equation is accepted.

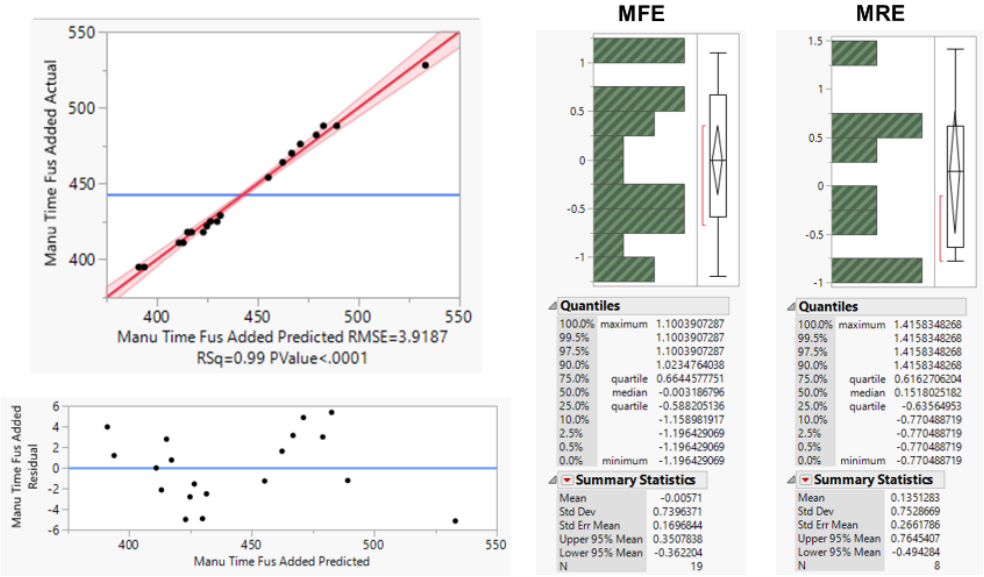

Figure 32: Agility driven vehicle manufacturing time regression

Agility driven hybrid VTOL vehicle manufacturing time regression

The change to VTOL adds the booms and the motor holders to the regression as shown in Figure 33.

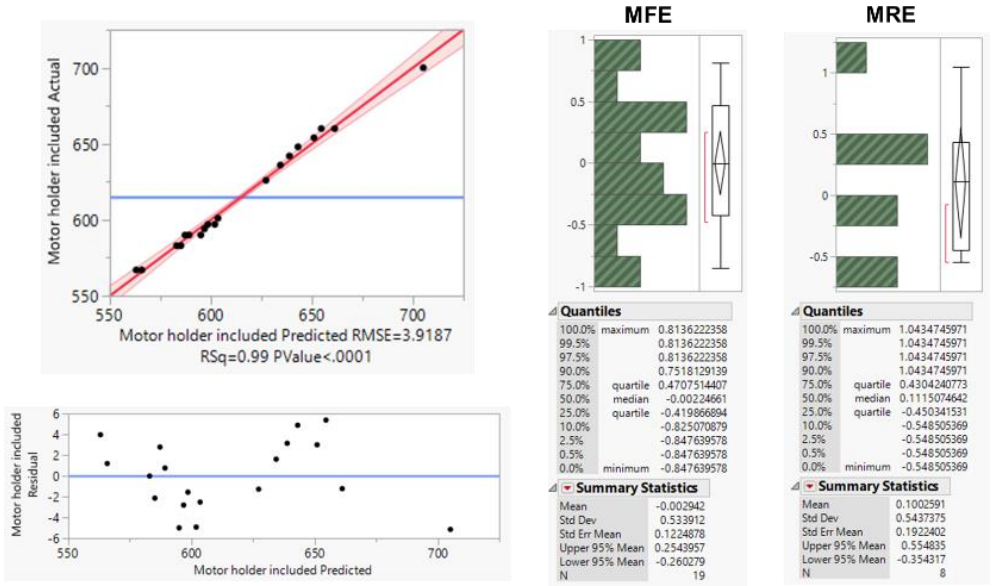

Figure 33: Agility driven VTOL vehicle manufacturing time regression

Payload driven vehicle manufacturing time regression

The payload driven design manufacturing time is fitted with a second order equation as shown in Figure 34.

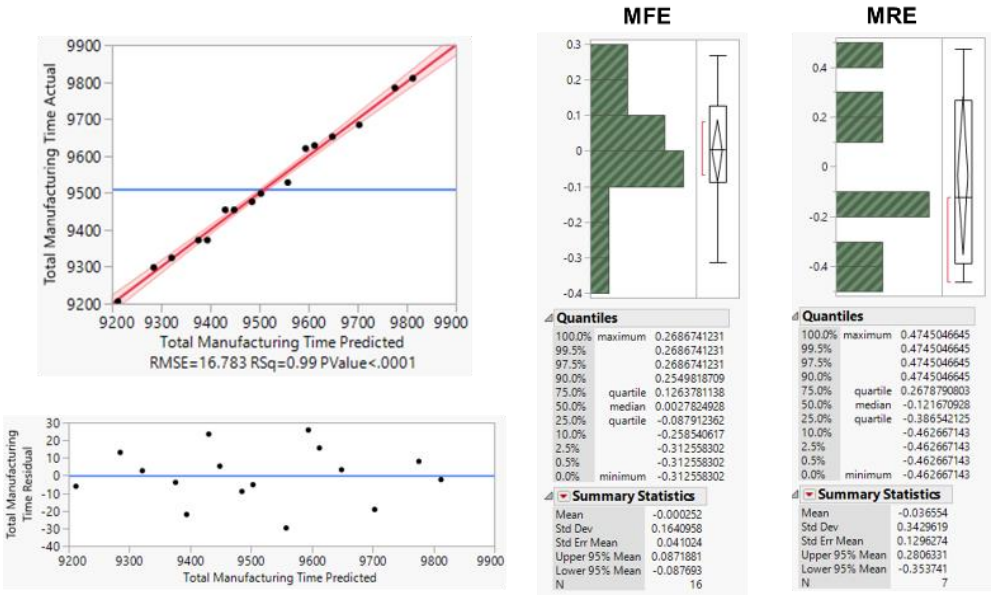

Figure 34: Payload driven vehicle manufacturing time regression

Payload driven hybrid VTOL vehicle manufacturing time regression

The payload driven VTOL is computed by an addition of booms and the motor holders as shown in Figure 27 and the results are given in Figure 35.

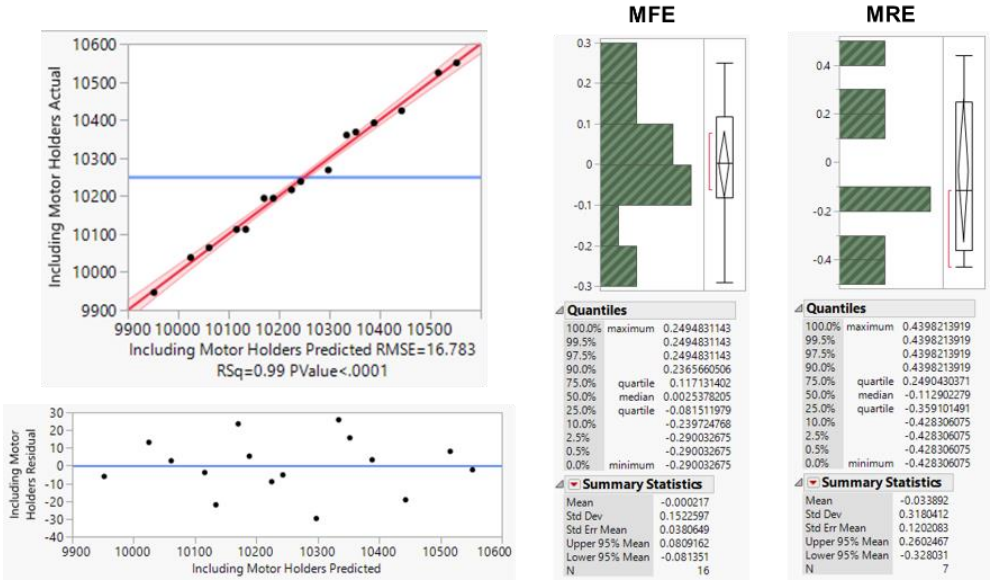

Figure 35: Payload driven VTOL vehicle manufacturing time regression

Quadcopter vehicle

For the quadcopter, the regression was previously performed and documented during the AEWE 2017 exercise. Two variants of the same quadcopter model are listed: one with top cover and the other with top plate. The regression results are shown in Figure 36 and Figure 37 respectively.

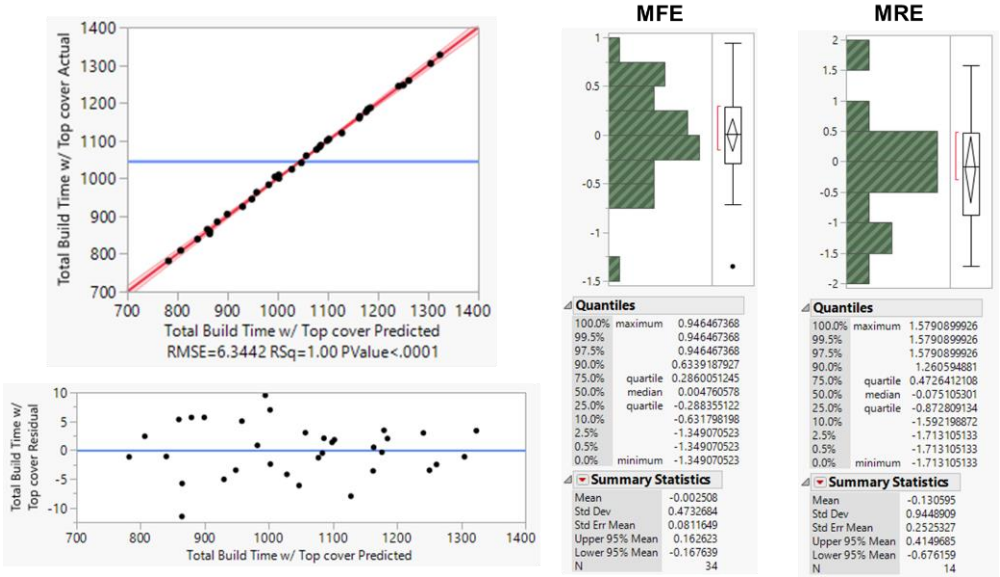

Figure 36: Manufacturing time regression for quadcopter with top cover

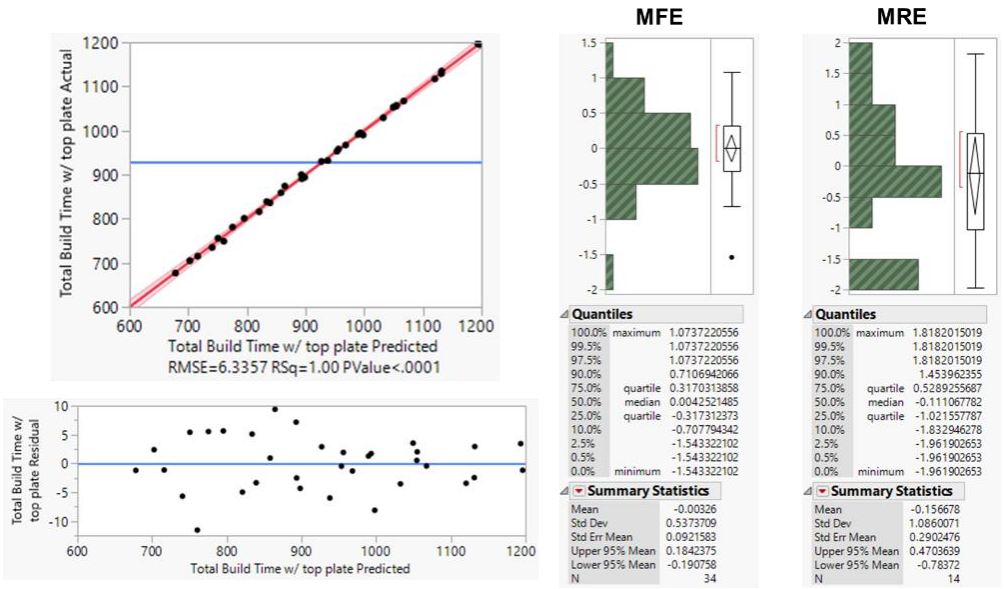

Figure 37: Manufacturing time regression for quadcopter with top plate

V. Visualization tradeoff and environment

Work regarding the integration of the models and the visualization environment was initiated early in the research and significant capabilities have been developed. This includes the ability to capture mission requirements as well as the capability to launch the analyses and the capability to display feasible design points in various graphs representing various metrics of interest to the analyst as shown in Figure 38. A cloud representation has also been developed using neighborhood analyses. This presents a more synthetic picture to the decision maker and help understand which areas of the design space and which areas of the capability space are attainable by each architecture under review. The cloud representation is also helpful in discovering Pareto fronts of non-dominated designs for a single type of architecture.

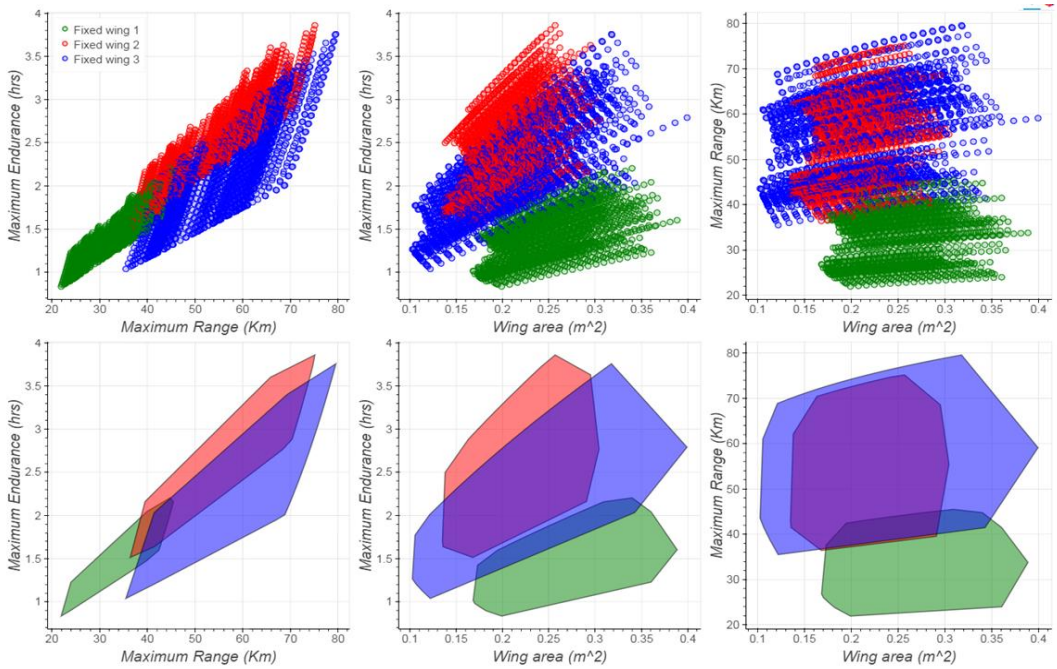

Figure 38: Feasible designs points in different capability spaces

Preliminary analyses were performed to identify the source of some of the trends and patterns highlighted in these graphs. For instance, the steep lines in Figure 39 represent different wing loadings for the same propulsion system (i.e. same battery, same propeller and same motor), while the shallower lines represent designs with a constant wing-loading but with an increasing battery capacity.

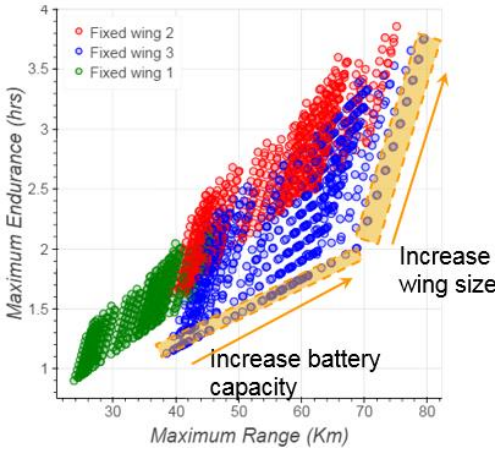

Figure 39: Explanation of some of trends and patterns seen in visualization environment

In order to facilitate these studies and present the user with as much useful information as possible, hovering capability for the mouse pointer has been developed. As a result, information pertaining to each and every of the designs represented in these graphs becomes available to the user by simply hovering over a feasible design point of interest. Information includes the type of propeller used, the type of motor used, the type of battery used, the vehicle weight, as well as the wing area if any. The visualization environment also include a function that enables a user to keep tracking a single design in multiple different metrics through highlighting the design point.

In the following sections, we will explain and demonstrate the visualization and user environment to show the capability of visualizing the analysis results. First, a general introduction of user environment and the components that comprised the environment are presented. Next, three major working tabs: mission information, visualization, and sensitivity analysis of the user environment are introduced and demonstrated with details. Last, an operation flow chart is provided indicating the sequence and the relationship between control function within and among the working tabs.

GUI Environment

General View

The user environment aims to provide users with an environment featuring friendly and intuitive experience to visualize, analyze, and convey information about interesting vehicle designs. Thus, users can identify the potential trade-off trends from the plots.

Elements of the GUI Environment

There are three major working components (tabs) in the user environment: Mission Information, Visualization, and Sensitivity Analysis. Each tab has several control functions and input options to handle

the visualized results. In Figure 40, Figure 41, and Figure 42 the layout for each working tab is presented. Detailed explanations and demonstrations are included in the following sections.

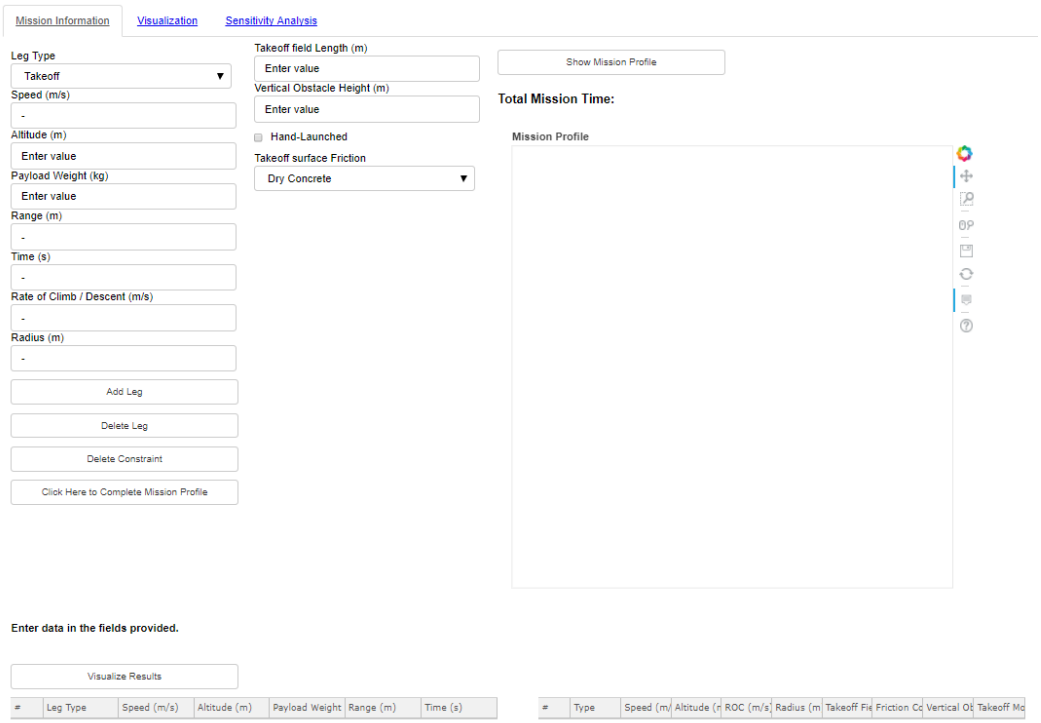

Figure 40: The working tab for mission information (before any computation)

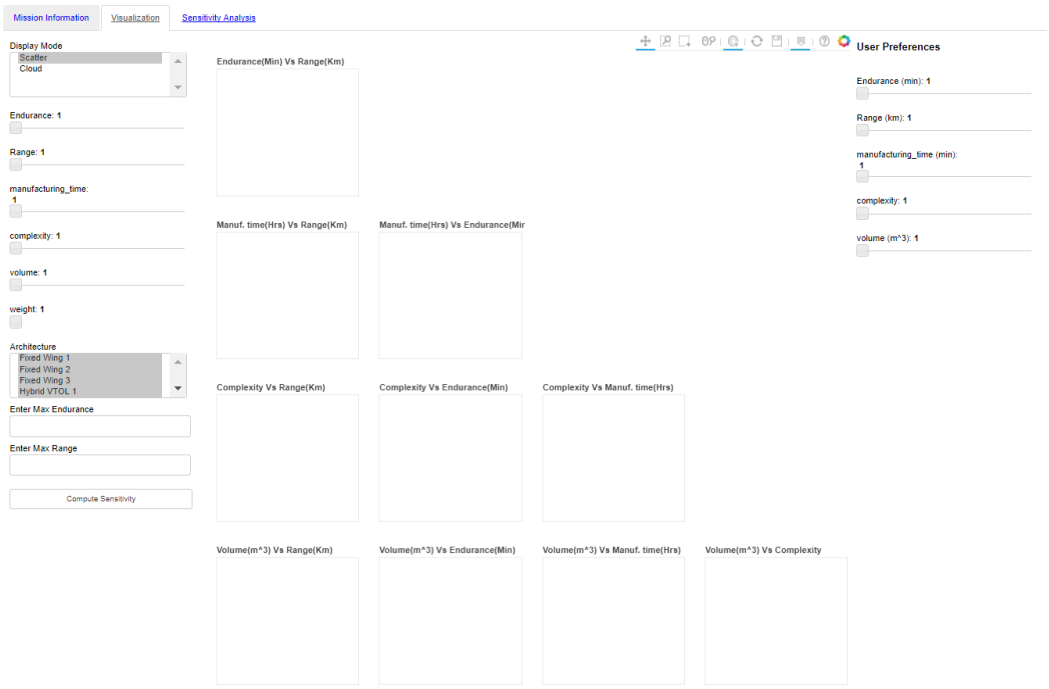

Figure 41: The working tab for visualization (Before any calculation)

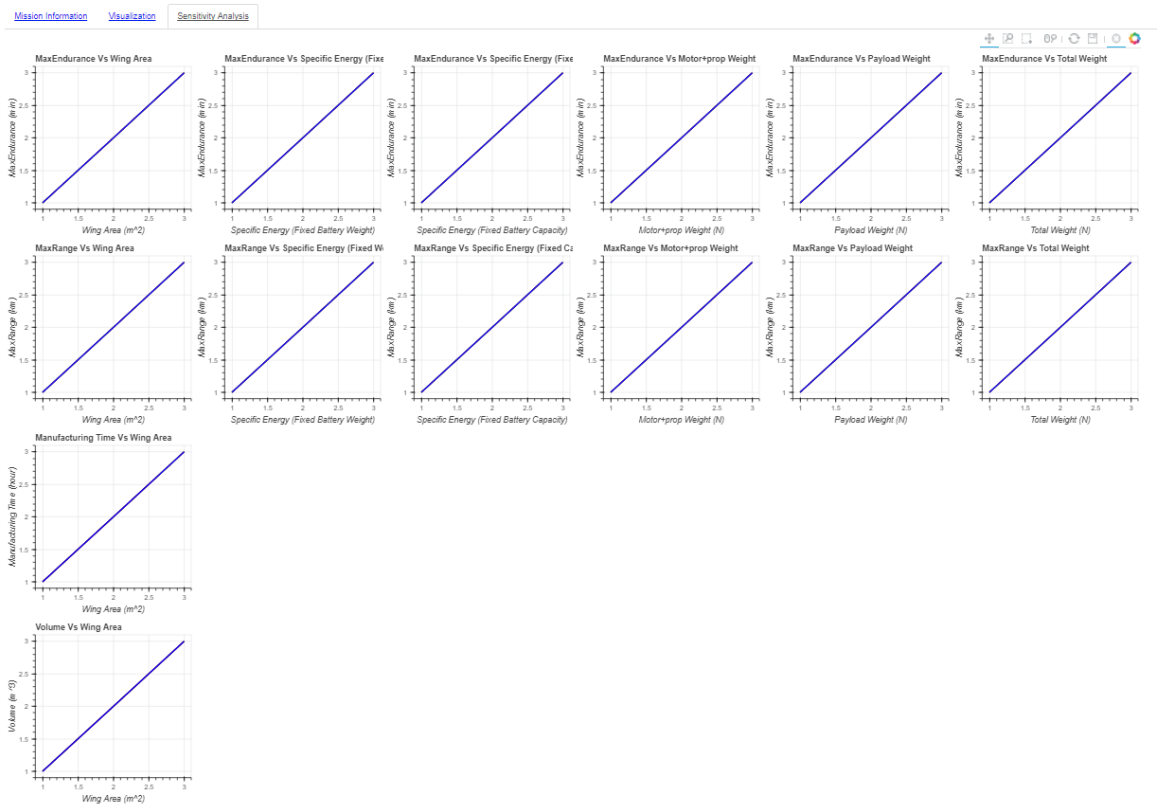

Figure 42: The working tab for sensitivity analysis (Before any calculation)

Operation Flow Chart

A flow chart for user operations within the GUI environment is presented in Figure 43 and it clearly shows the relationship between the three working tabs. With the support of this chart, the analyst can implement the visualization environment efficiently and look-up for detailed explanations for each of the control functions within each working tab that were described in the previous sections.

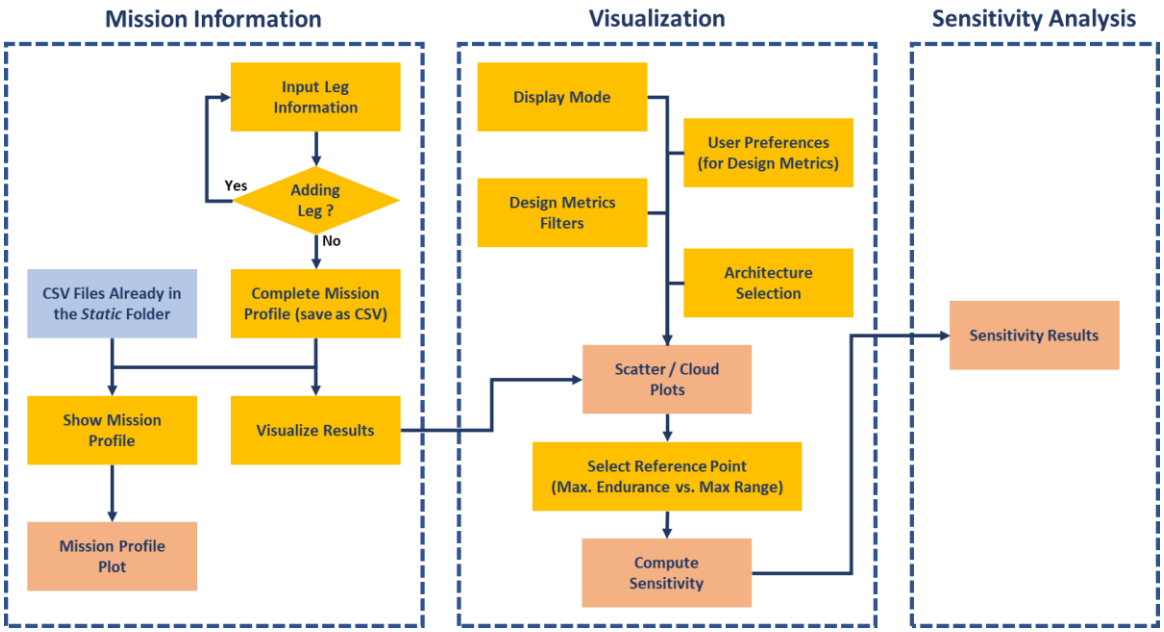

Figure 43: Operation flow chart for user environment

Mission Information

This Mission Information tab is where the analyst can input design mission information that will be used for sizing and synthesis calculations. The tab also summarizes and provides a visualization of the mission profile and mission constraints. Next, the Mission Information tab is decomposed into different subsections.

Basic Input for Sizing and Synthesis

Figure 44 shows blocks and controls to collect basic information for the sizing and synthesis. The "Leg Type" dropdown selection allows the user to decide the type of current leg. Another dropdown window "Takeoff Surface Friction" provides several surface conditions for the takeoff operations. Other blocks (Such as Speed, Altitude, Payload ... etc.) must be filled according to the instruction inside the block. For example, in Figure 44, inside the "Speed" block, there is a "-" sign, which means that no value is expected for the takeoff leg. On the other hand, if the instruction inside the block indicates "Enter value", then a value must be assigned.

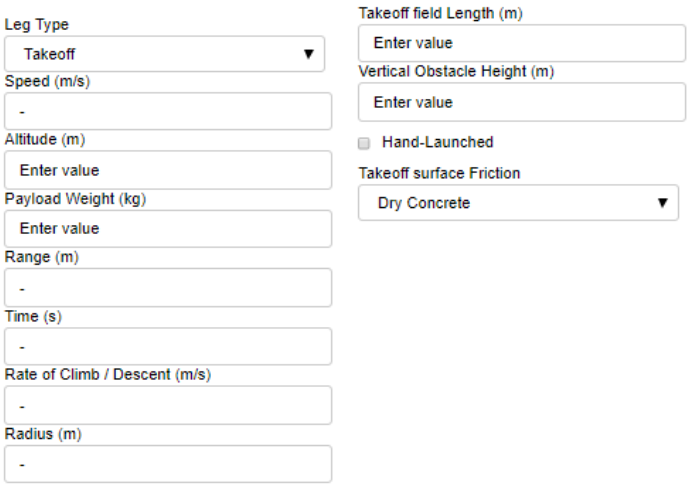

Figure 44: Blocks and functions for basic sizing and synthesis inputs

Adding Legs and Saving the Mission Profile/Mission Constraint Information

Once the input of information for the current leg is complete, users may continue to add or delete other leg information by clicking the "Add Leg" or "Delete Leg" button. A constraint can also be deleted by clicking "Delete Constraint". Once all the mission information (all the legs and constraints) is entered, the information about mission profile and mission constraints can be stored in the folder named ***static*** as a .CSV files by clicking button "Click Here to Complete Mission Profile". All the buttons and functions are presented in Figure 45.

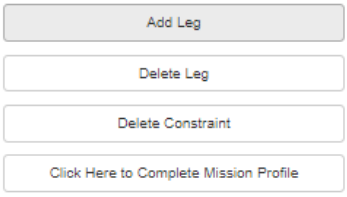

Figure 45: Control buttons for adding legs and saving/changing the input information

Show Mission Profile

By clicking the *Show Mission Profile* button, two windows will pop-out; the first one is for the mission profile as shown in Figure 46 and the second one is for the mission constraints as shown in Figure 47. They invite the user to select two files that should already exist in the static folder, either through the manual input process mentioned in previous subsection that created these two files, or by having been prepared in advance and saved to the folder previously. Figure 48 shows the picture of the mission profile

before and after any mission files (mission profile/mission constraints) were selected. Also, after the mission files were chosen, a table contains information of mission profile and mission constraints will also appears at the bottom of Mission Information tab, as shown in Figure 49.

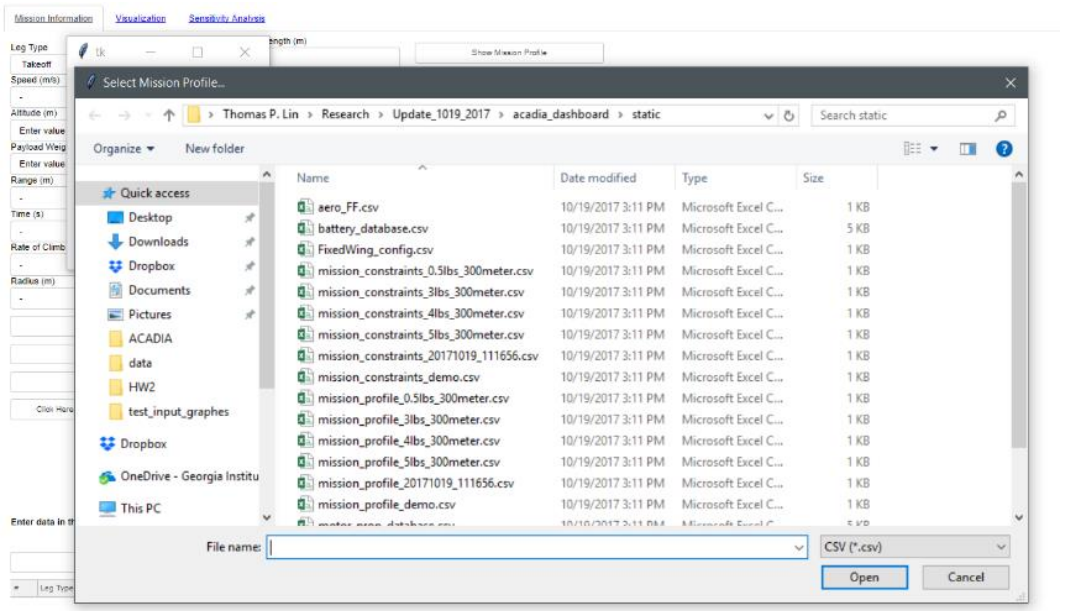

Figure 46: Pop-out window for selecting the mission profile

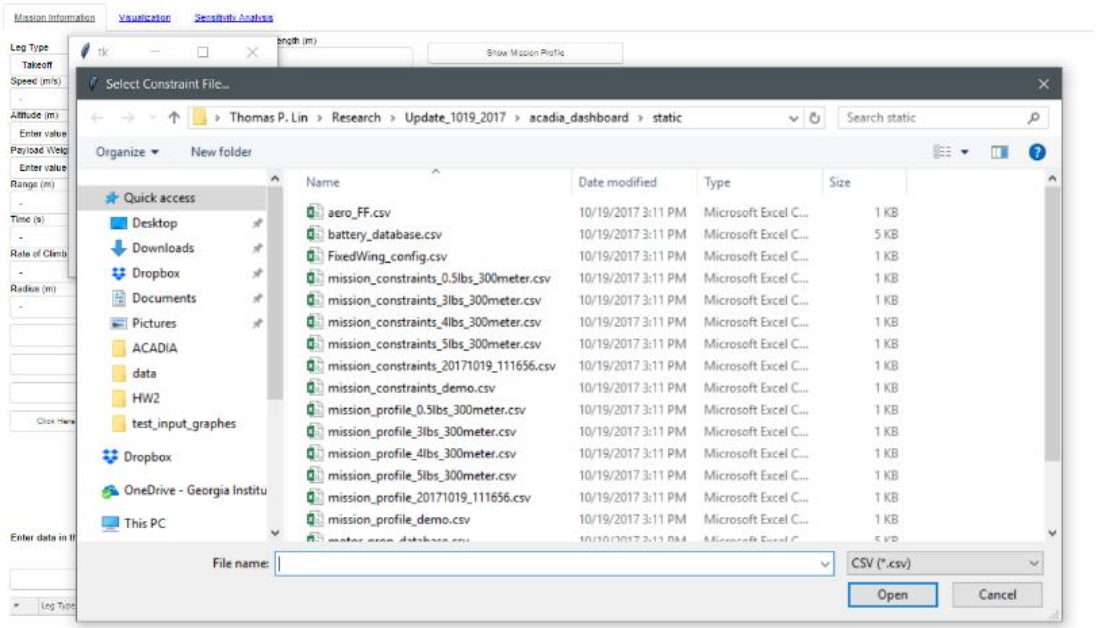

Figure 47: Pop-out window for selecting the mission constraints

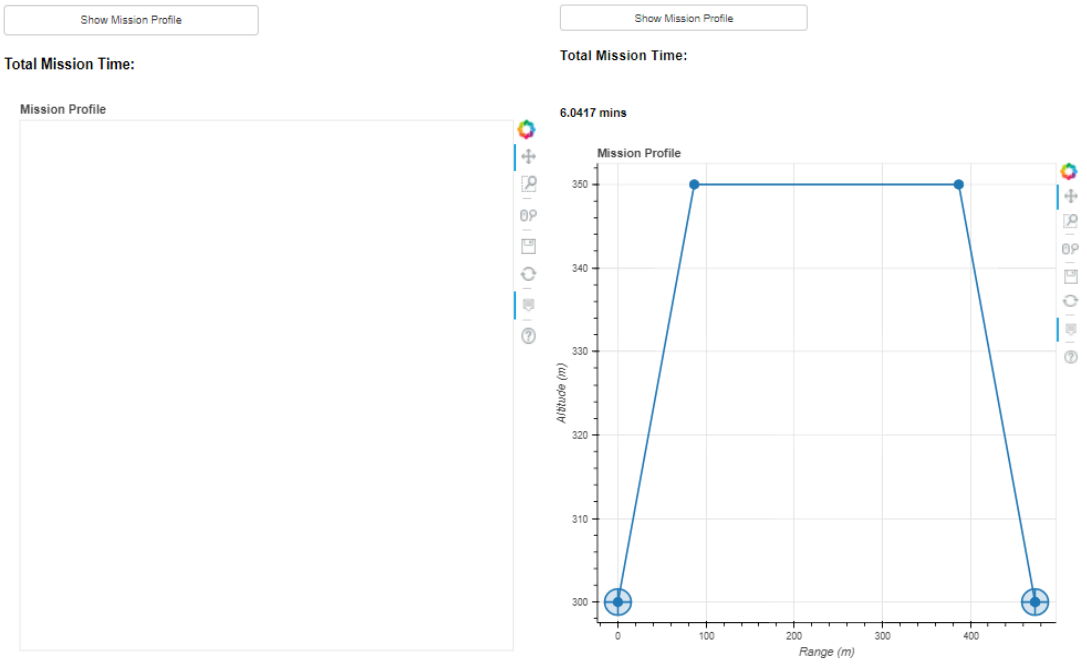

Figure 48: Mission profile plots (Before and after the selection of mission profile and constraints)

#	Leg Type	Speed (m/s)	Altitude (m)	Payload Weight	Range (m)	Time (s)
0	Takeoff	-	300	0.22	-	-
1	Climb	8	350	0.22	288	-
2	Cruise	8	350	0.22	300	-
3	Descent	8	300	0.22	300	-
4	Land	-	300	0.22	-	-

#	Type	Speed (m	Altitude (r	ROC (m/s	Radius (m	Takeoff Fie	Friction Co	Vertical Ob	Takeoff Mo
0	Takeoff	-	300	-	-	100	0.5	2	Ground...
1	Climb	8	350	2	-	-	-	-	-
2	Cruise	8	350	-	-	-	-	-	-

Figure 49: Tables for mission profile and mission constraints

Visualize Results

To do the sizing and synthesis calculation and to visualize the results of this exercise, the user should click the button "*Visualize Results*" executing therefore the calculation process. After clicking the button, two pop-out windows will also appear that are identical to the two windows shown in Figure 46 and Figure 47. Select the corresponding mission files, and the status for computation process will appear above the button. Figure 50 demonstrates the computation status change.

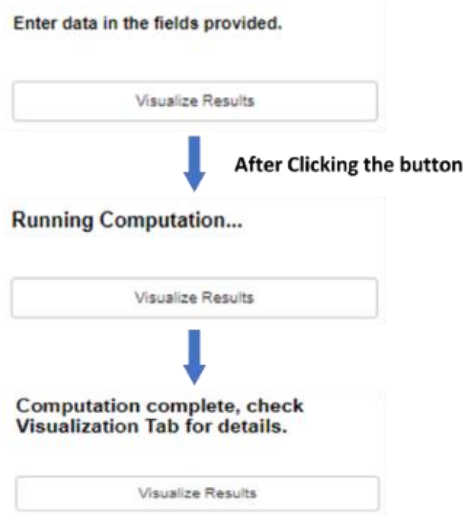

Figure 50: Computation status indicator

After completion of mission profile and mission constraints inputs and after performing the sizing and synthesis exercise, a visualization environment for the results is presented in the working tab of "Visualization".

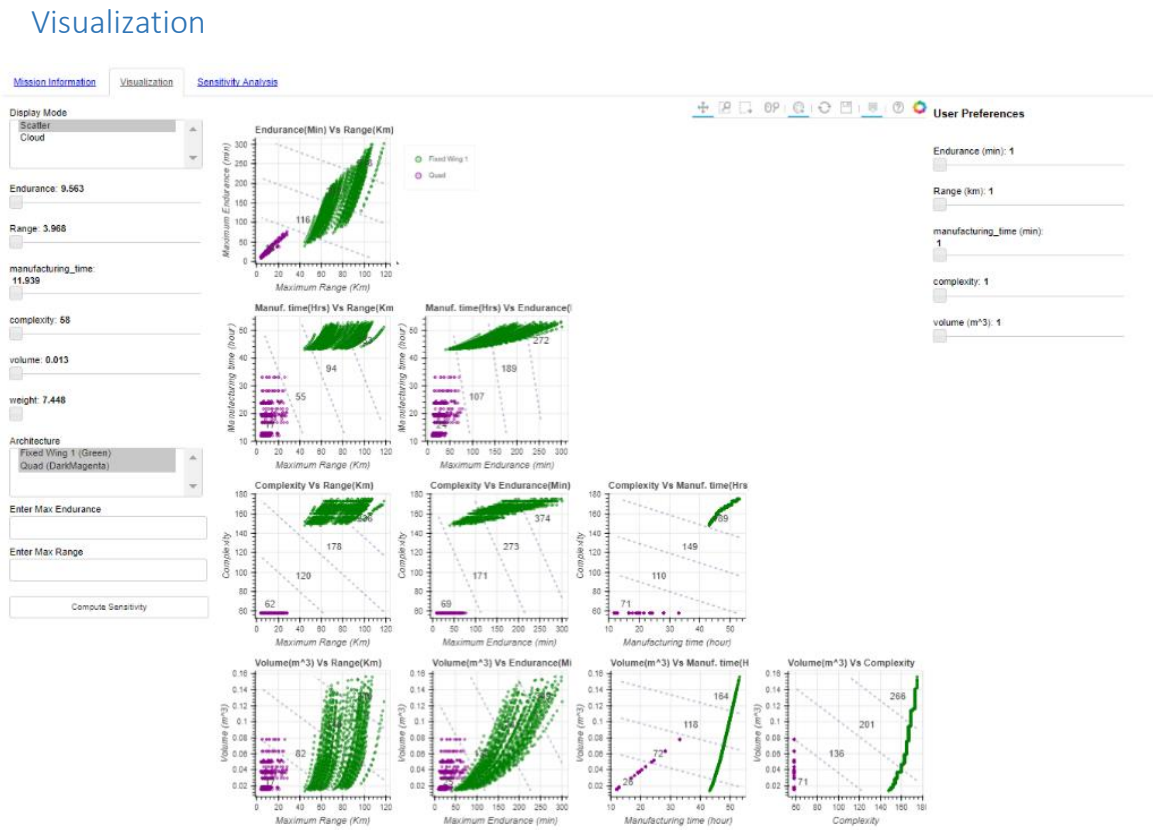

Figure 51: The visualization of sizing and synthesis results

After clicking the button “Visualize Results”, the results will appear in “Visualization” working tab as shown in Figure 51. Using the control functions on the “Visualization” tab, we can easily manipulate the design metric plots by adjusting design metric filters, display mode, architecture selection, and user preferences to highlight design points that may be of interest. The following subsections focus on the control interfaces inside the *“Visualization”* working tab, and the three top-left corner design metric plots will be used as examples to demonstrate how these controls affect the visualization results.

Display Mode

Figure 52: Layout for display mode

By default, the visualization results are all in “Scatter” mode as shown in Figure 53.

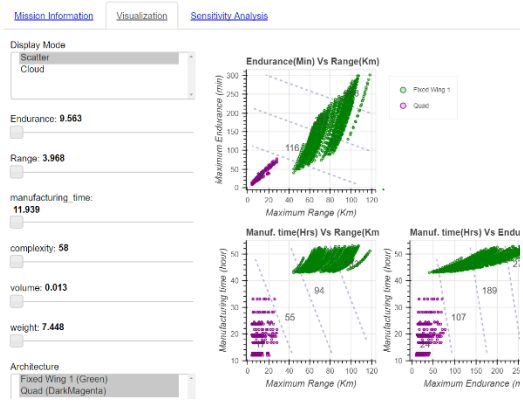

Figure 53: Plots in scatter mode

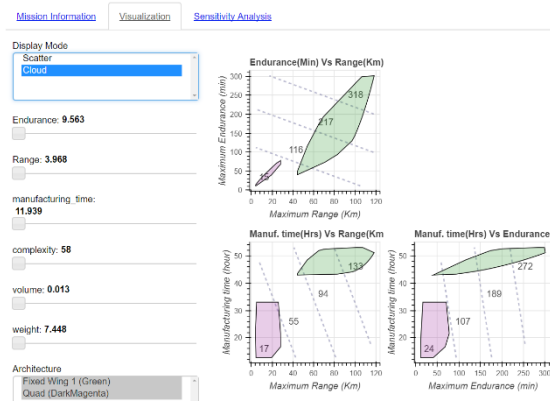

Figure 54: Plots in cloud mode

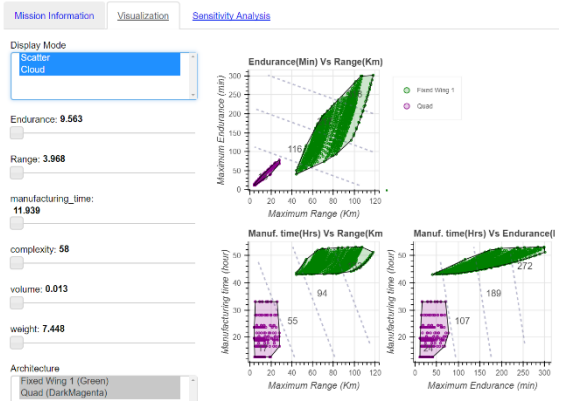

Figure 55: Plots in both scatter and cloud mode

Now, if the user clicks *"Cloud"* inside *"Display Mode"* block, the visualized results will turn into cloud plots as shown in Figure 53. This makes the discovery of architecture-specific Pareto front easier to make. Moreover, the *"Display Mode"* control allows the user to display the information as both a scatterplot mode and a cloud mode at the same time in one plot, as displayed in Figure 53. With these different display modes, the user can extract the trends and distributions of design points for each architecture. By hovering the mouse over any design point, an information window appears on the plot and it provides a lot of information about the design and its neighboring designs.

Architecture Selection

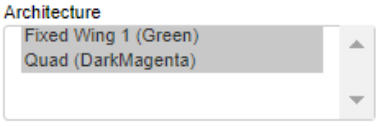

Figure 56: Layout for architecture selection

By selecting the architecture type inside the *"Architecture Selection"* block, the user can filter the plots and highlight only specific architectures. Figure 57 to Figure 59 are providing a demonstration of this function. This control allows the user to focus on the architecture of interest.

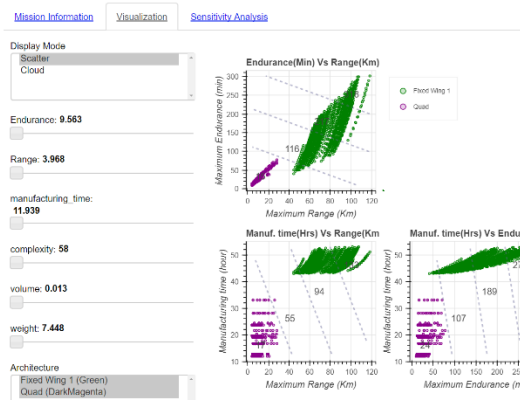

Figure 57: Plots with both architectures

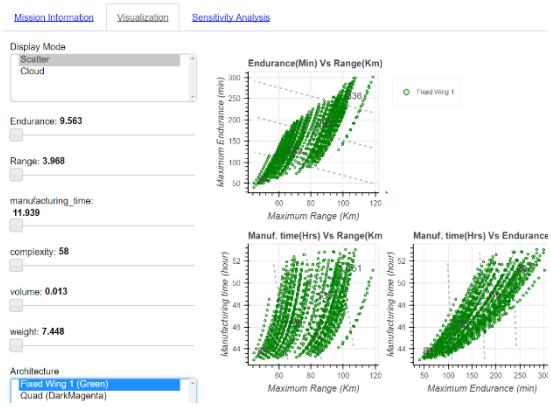

Figure 58: Plots only for fixed wing designs

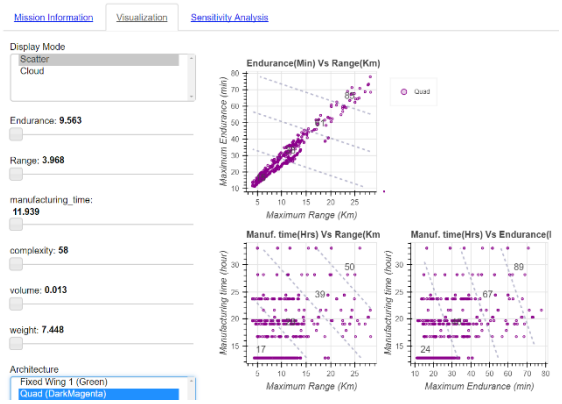

Figure 59: Plots only for quadcopter designs

Design Metrics Filters

To down select and highlight specific design points, metrics filters can be used by the analyst to narrow down the range of designs being displayed. Figure 60 presents the layout for the metric filters and the control of these filters is demonstrated in Figure 61 to Figure 63. In Figure 61, the architecture is fixed wing and the display mode is in scatter mode. The settings for design metric filters are on the right (Endurance: 9.5 min; Range: 3.9 km). Now, if the "Endurance" filter is adjusted first, from 9.5 min to 155.3 min, the lower bound of the vertical axis of Maximum Endurance vs. Maximum Range plot are changed from 30 min to around 155 min and it shows only design with a maximum endurance longer than 155.3 min. This is demonstrated in Figure 62

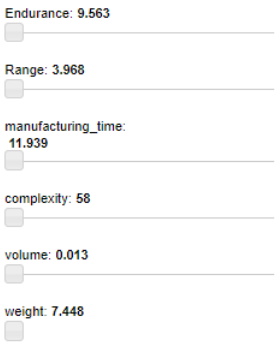

Figure 60: Layout for design metric filters

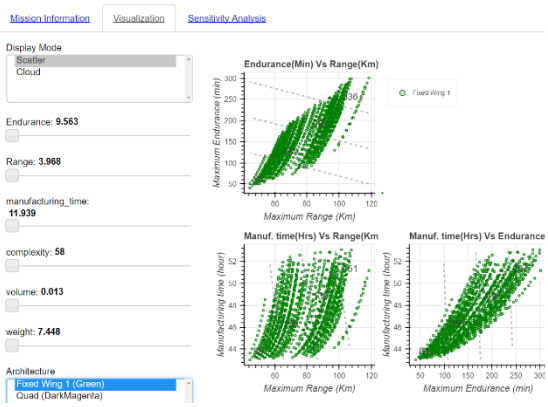

Figure 61: Default setting of filters

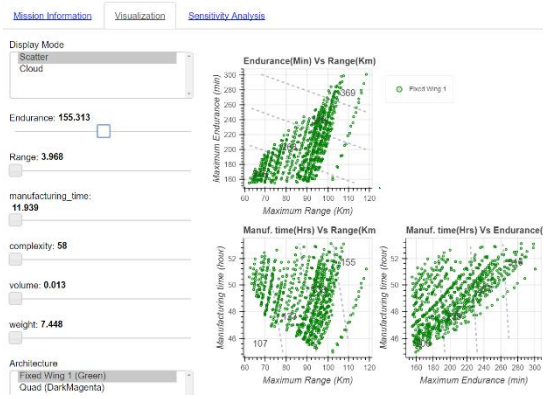

Figure 62: Set Endurance to a value (155.3 min)

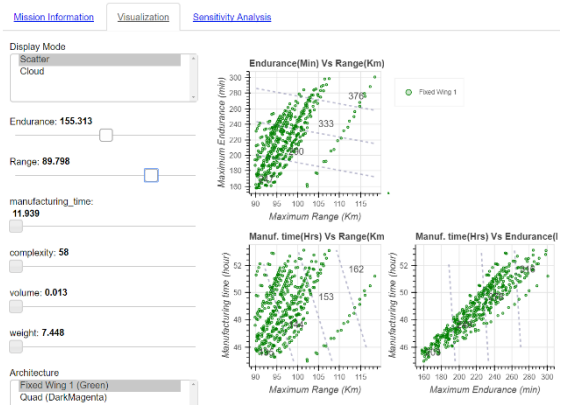

Figure 63: Set Endurance (155.3 min) and Range (89.9 km)

Figure 63 shows the filtered results when the endurance filter is set to 155.3 min and the range filter is set to 89.7 km. With the support of design metric filters, the analyst can easily reduce the number of design point to be displayed to focus on specific areas of the design space / capability space.

User Preferences

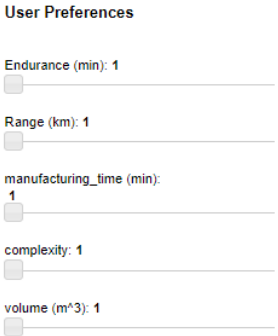

Figure 64: Layout for user preferences

The User Preferences functionality allows the user to visualize the gradient for the various design metrics retained. In other words, it represents the overall direction of improvement taking into account the user preferences. It is represented by gray dashed lines on the design metrics plots. Using these gray dashed lines, the search direction for finding desirable improvements can be highlighted. Also, the search directions for these design metrics are perpendicular to the dashed line. The user preference can be adjusted by changing the relative weight of the design metrics (higher/lower value for the design metric weight indicates higher/lower "preference" for the design metric) as shown in Figure 64. In turn, this changes the slope of the gradient lines as demonstrated in Figure 65 and Figure 66. In the case of Figure 66, the relative weight of range (Maximum Range) is adjusted from 1 to 5 indicating that ranges becomes progressively more desirable.

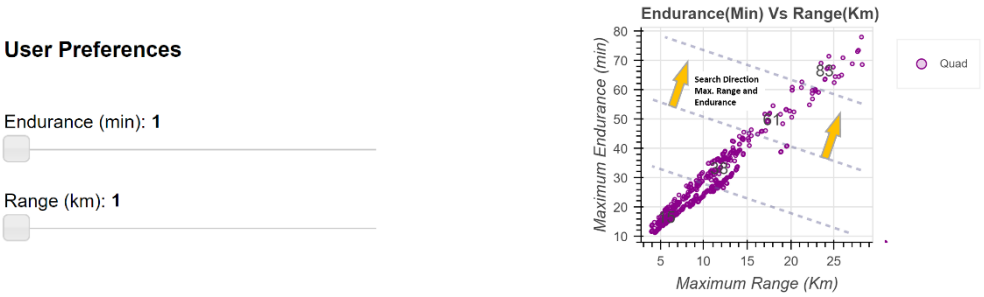

Figure 65: User preference for Endurance and Range set in default weight values

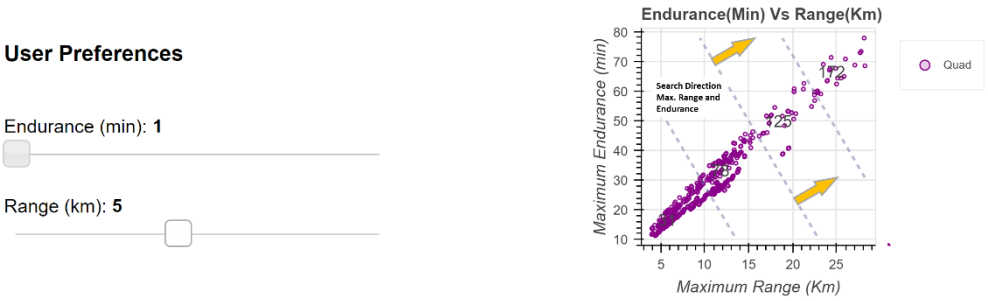

Figure 66: Setting the weight of Range to 5 and keeping Endurance to 1 in the user preference

By adjusting the *range* relative weight (preference), the search direction that looks for the best maximum endurance and best maximum range among design points is changed accordingly. Compared to the results in Figure 65, the search direction in Figure 66 is changed and the direction for improvement is shallower indicating that more desirable areas of the design space are towards the right side of the graph.

Sensitivity Analysis

The last working tab provides visual results for the sensitivity analysis. The purpose of the sensitivity analysis is to highlight how sensitive or how robust the different architectures are with respect to technical or technological assumptions. For instance, this can help the analyst understand whether improvements in battery technologies will have a more significant impact on the performance of the vehicle for a fixed wing vehicle or for a quadcopter vehicle. These sensitivities are expressed is various dimensions as shown by the various graphs in Figure 68.

To perform sensitivity analyses, the user needs to choose a reference point or a reference neighborhood in the Maximum Endurance vs. Maximum Range plot first so that sensitivities are performed in a specific area of the design space. Once this area is chosen, the user enters the corresponding maximum endurance and maximum range values in the blocks located at the bottom-right corner of the working tab *"Visualization"*, as shown in Figure 67. Next, the python code, main.py, will choose design points closest to this specific neighborhood for each of the architectures under review in order to perform sensitivity studies. The results are presented in Figure 68. It is worth mentioning that for these sensitivity studies the vehicles are not resized.

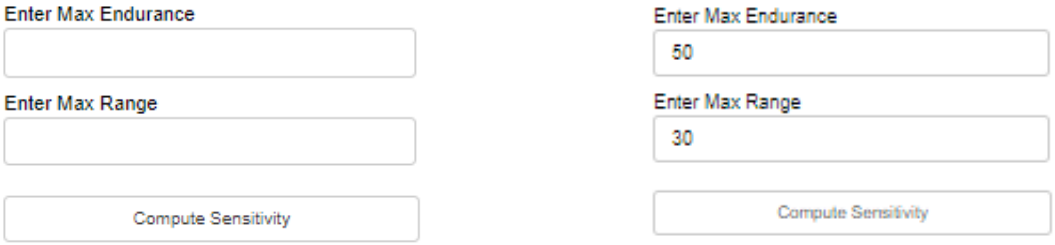

Figure 67: Entering values for reference//neighborhood area to perform sensitivity analyses

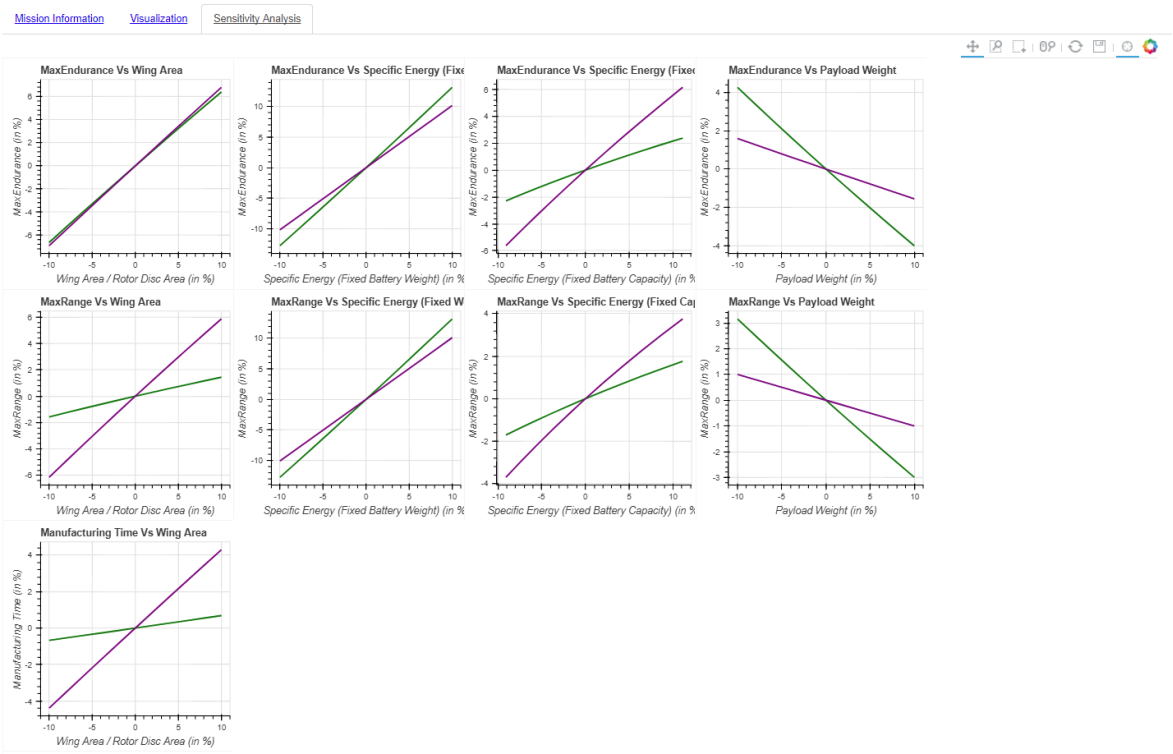

Figure 68: Sensitivity results for design metrics (Maximum Endurance, Maximum Range, Manufacturing Time, and Volume) to design parameters (wing area, specific energy of battery, motor and propeller weight, payload weight, and total weight).

In Figure 68, several sensitivity plots using five different and uncertain design parameters are displayed (there are two sensitivity plots for the battery specific energy, one for a fixed battery weight scenario and the other one for a fixed battery capacity scenario). To get sensitivity curves, the design parameter of interest is perturbed by about $\pm 10\%$ from its original value and the different metrics are recalculated using this new value for the parameter while keeping all other inputs constant. The sensitivity curves are also color coded according to the design architecture represented (in the demonstration case, green is for one fixed wing architecture while dark magenta is for quadcopter). Finally, all the sensitivity results are normalized to their original baseline values and represented as percentages to indicate and compare the sensitivity of the responses.

References

[1] Mattingly, J. D., Heiser, W. H., and Daley, D. H., Aircraft engine design. AIAA, 1989.

[2] Nam, T., Soban, D. and Mavris, D., *A generalized aircraft sizing method and application to electric aircraft,* 3rd International Energy Conversion Engineering Conference (p. 5574), 2005

[4] Anderson, J. D., *Aircraft performance and design*, Boston: WCB/McGraw-Hill, 1999.

[5] Traub, L. W., *Range and Endurance Estimates for Battery-Powered Aircraft*, Journal of Aircraft, vol. 48, 2011, pp. 703–707.

[6] Leishman, G. J., *Principles of Helicopter Aerodynamics*, 2nd Ed., New York, NY, Cambridge Aerospace Series, 2006

[7] Prouty, R. W., *Helicopter Performance, Stability, and Control*, 2nd Ed., Malabar, FL, Krieger Publishing Company, 2002

[8] Willard, N., *Multicopter Aerodynamics*, Unpublished Report, Experimental tests performed at the Georgia Institute of Technology, 2016